LITHOS 398-399 (2021) 106355

Contents lists available at ScienceDirect

LITHOS

journal homepage: www.elsevier.com/locate/lithos

Research Article

Petrology and geochemistry of early Permian mafic–ultramafic rocks in the Wajilitag area of the southwestern Tarim Large Igneous Province: Insights into Fe-rich magma of mantle plume activity

Sheng-Zhu Zhu [a,b,c,d], Xiao-Long Huang [a,b,c,*], Fan Yang [a,b,c], Peng-Li He [a,b,c]

[a] State Key Laboratory of Isotope Geochemistry, Guangzhou Institute of Geochemistry, Chinese Academy of Sciences, Guangzhou 510640, China
[b] CAS Center for Excellence in Deep Earth Science, Guangzhou 510640, China
[c] Southern Marine Science and Engineering Guangdong Laboratory (Guangzhou), Guangzhou 511458, China
[d] University of Chinese Academy of Sciences, Beijing 100049, China

ARTICLE INFO

Keywords:
Magmatism
Fe-rich magma
Fe–Ti-oxide deposit
Recycled oceanic crust
Large igneous province
Mantle plume

ABSTRACT

The majority of global Fe–Ti-oxide deposits hosted in mafic–ultramafic layered intrusions are closely related to mantle plume activity. The metallogenesis of these Fe–Ti-oxide deposits is still debated, especially with regard to their mantle source and relationship to magmatism. Here we report detailed petrology and geochemistry for early Permian (ca. 280 Ma) mafic–ultramafic igneous rocks in the Wajilitag area of the western Tarim Large Igneous Province (TLIP) to establish the relationships among mantle source, magmatism, and metallogenesis in mantle plume activity. The mafic rocks (i.e., gabbro and diabase) show alkaline affinities and OIB-like trace-element patterns. Clinopyroxenites closely related to Fe–Ti-oxide deposits were derived from the same magmatic system as that of the mafic rocks. The primary magma of the Wajilitag mafic rocks was enriched in FeO^T and TiO_2 and depleted in SiO_2, and has high FC3MS ($FeO^T/CaO - 3MgO/SiO_2$) and Fe/Mn, indicating the involvement of Si-poor pyroxenite/eclogite in the mantle source. Primary olivines from the Wajilitag gabbro have consistently high NiO and Fe/Mn. Wajilitag mafic rocks have variable Sr–Nd–Hf isotopes owing to their derivation from a hybrid mantle source with the involvement of subducted oceanic crust and sediments. Subducted slabs within the upper mantle are inferred to have been entrained by the upwelling mantle plume and preferentially melted to produce mainly Fe-rich magma. The occurrence of an adjacent oceanic subduction event just prior to the operation of a mantle plume played a crucial role in the formation of large-scale Fe–Ti-oxide deposits in LIPs.

1. Introduction

Mantle plumes drive the chemical differentiation of the solid Earth. A main outcome of a plume interacting with the lithosphere is the formation of large igneous provinces (LIPs), a process that is usually accompanied by extensive magmatism (e.g., He et al., 2016; Xiao et al., 2004) and mineralization events (e.g., Namur et al., 2010; Zhong et al., 2011). Specifically, the majority of world-class Fe–Ti-oxide deposits hosted in mafic–ultramafic layered intrusions are closely related to LIP events caused by mantle plume activity, such as the Bushveld intrusion in South African (Wilson, 2012), the Panzhihua intrusion in southwestern China (Zhong et al., 2011), the Sept Iles intrusion in Canada (Higgins and van Bremen, 1998), the Skaergaard complex in Greenland (Tegner et al., 1998), and the Duluth complex in the USA (Chalokwu et al., 1996). However, some LIPs, including the Siberian and Deccan LIPs, lack large-scale Fe–Ti-oxide deposits, although they also were related to plume activity (Haase et al., 2019; Saunders et al., 2005).

Numerous studies have proposed that processes of magmatic evolution, such as crystallization fractionation (Song et al., 2013; Toplis and Carroll, 1995), silicate-oxide liquid immiscibility (Charlier et al., 2011), and magma–carbonate interaction (Tang et al., 2021), are important to the generation of Fe–Ti-oxide deposits. However, the role of magmatic processes in producing Fe–Ti-oxide deposits is less particular to the region involved but is more dependent on the physical and chemical features of the magma (Philpotts, 1982; Whitaker et al., 2007 and references therein). Thus, whether an LIP has large-scale Fe–Ti-oxide deposits should be independent of magmatic evolution. Fe–Ti-rich primary magma might be an important control on the generation of large-scale

* Corresponding author at: State Key Laboratory of Isotope Geochemistry, Guangzhou Institute of Geochemistry, Chinese Academy of Sciences, Guangzhou 510640, China.
E-mail address: xlhuang@gig.ac.cn (X.-L. Huang).

https://doi.org/10.1016/j.lithos.2021.106355
Received 13 March 2021; Received in revised form 11 June 2021; Accepted 7 July 2021
Available online 10 July 2021

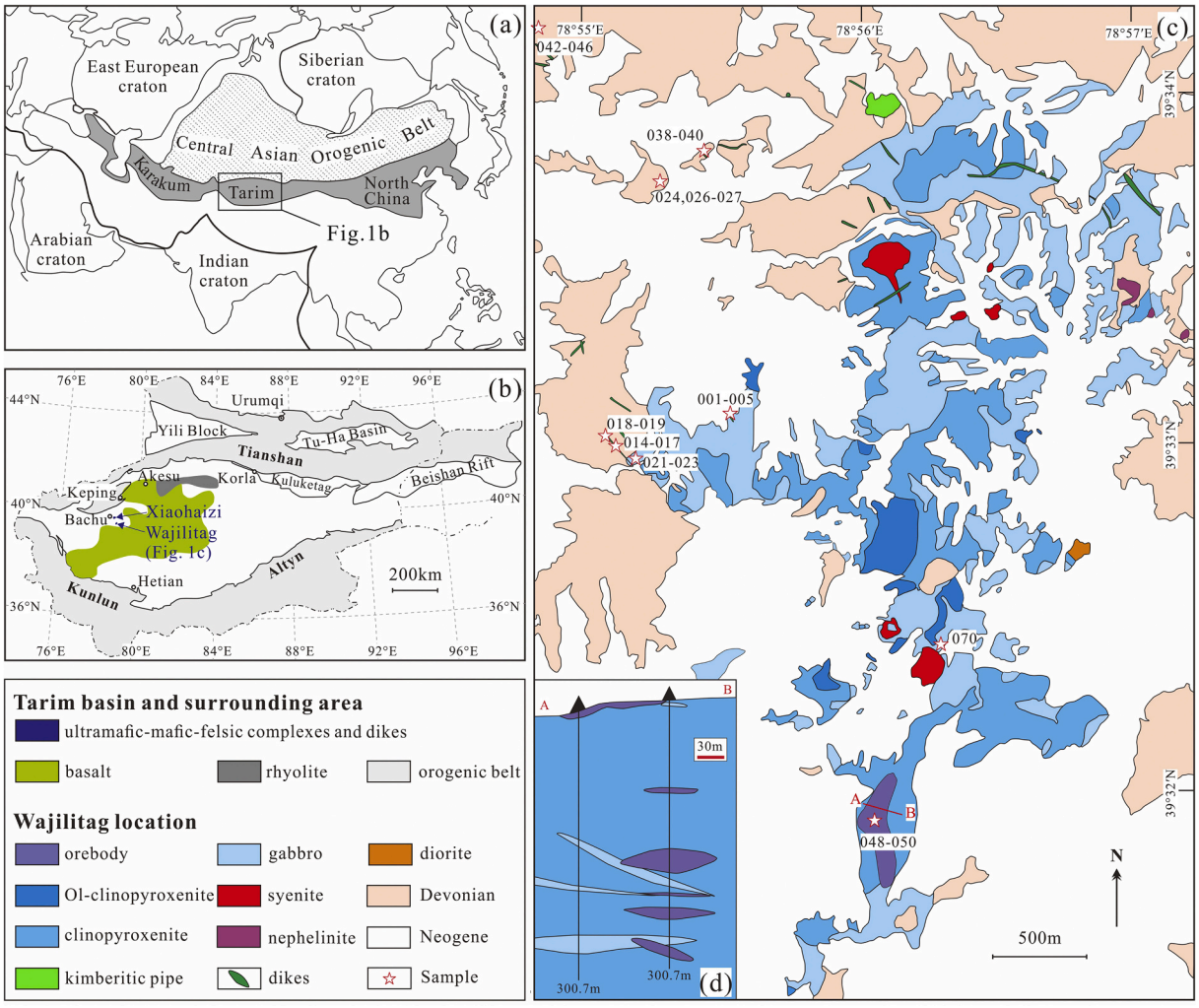

Fig. 1. (a) Schematic map showing the position of the Tarim Craton, modified after He et al. (2016); (b) simplified tectonic map of the Tarim Basin, modified after Wei et al. (2014) and Xu et al. (2014); (c) simplified geological map of the Wajilitag area showing the distribution of early Permian igneous rocks and sample locations, modified after Cheng et al. (2015), Zou et al. (2015), and Zhang et al. (2016); and (d) cross section of the Wajilitag complex, with investigated drill holes, modified after Zhang et al. (2018).

Fe–Ti-oxide deposits in LIPs because such magma can enhance the reserves of ore deposits (Bai et al., 2014). In general, Fe-rich primary magmas are derived from an Fe-rich mantle source (Gibson et al., 2000), such as garnet pyroxenite (Tuff et al., 2005) and Fe-rich peridotite (Gibson, 2002; Gibson et al., 2000). Garnet pyroxenite might be related to subducted oceanic lithosphere becoming entrained by an upwelling plume and reacting with surrounding peridotite (Tuff et al., 2005), whereas Fe-rich peridotites are formed by mixing and reaction processes between convecting mantle peridotite and subducted oceanic crust (Gibson, 2002; Gibson et al., 2000). Thus, the involvement of recycled oceanic crust in the mantle source may account for the metallogenesis of large-scale Fe–Ti-oxide deposits in LIPs (Bai et al., 2014; Tang et al., 2021). Because an upwelling mantle plume could entrain recycled oceanic crust from the deep mantle and even the core–mantle boundary (Hofmann and White, 1982), pyroxenites are a common lithology in the mantle source of almost all plume-related basaltic rocks (Lambart et al., 2013). Therefore, the key issue is whether pyroxenites (recycled oceanic crust) have a particular composition and genesis that favor the production of large-scale Fe–Ti-oxide deposits in LIPs.

Early Permian mafic–ultramafic rocks in the Wajilitag area in the western margin of the Tarim Craton, including mafic dikes, mafic–ultramafic intrusions, nephelinites, and kimberlitic rocks, are all rich in total FeO (FeO^T; Zhang et al., 2010, 2013, 2018; Cao et al., 2014, Cheng et al., 2015) and have been considered typical magmatic rocks of the Tarim LIP (TLIP; Fig. 1; Xu et al., 2014). A large-scale Fe–Ti-oxide deposit in the Wajilitag area has also been suggested to be associated with the Tarim mantle plume (Cao et al., 2014; Xu et al., 2014; Zou et al., 2015). Thus, igneous rocks of the Wajilitag area favor an investigation of the metallogenesis of Fe–Ti-oxide deposits with respect to mantle plume activity. Although previous studies have examined aspects such as the geochronology and geochemistry of Wajilitag mafic–ultramafic rocks (Cao et al., 2014; Zhang et al., 2008; Zou et al., 2015), the mantle sources of these rocks are still uncertain and might include lithospheric mantle (Zhang et al., 2016, 2018) or asthenospheric mantle (Cao et al., 2014). In this study, we report a comprehensive investigation into the petrology, mineralogy, geochemistry, and geochronology of early Permian mafic–ultramafic rocks in the Wajilitag area, including mineralized clinopyroxenite, gabbro, and diabase, with the aim of gainning an insight into the magma sources, melt generation, and subsequent evolutionary processes involved in the formation of these rocks. We propose that the subduction history in the area adjacent to an LIP is a crucial factor controlling the generation of large-scale Fe–Ti-oxide deposits during mantle plume activity.

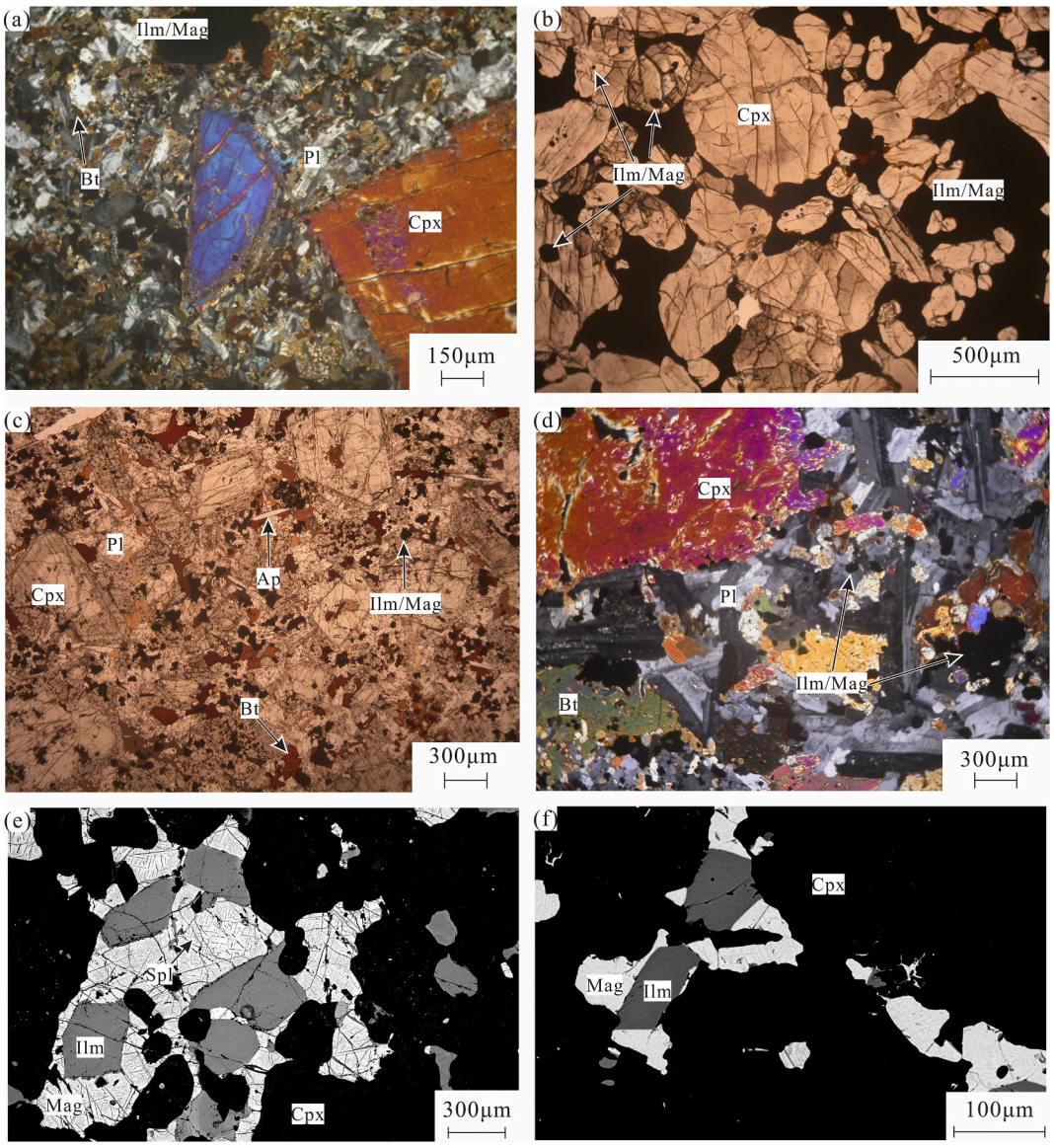

Fig. 2. Photomicrographs and backscattered electron (BSE) images of Wajilitag mafic–ultramafic rocks: (a) diabase showing typical ophitic structure with clinopyroxene phenocrysts; (b) cumulatic texture of mineralized clinopyroxenite, with mostly ilmenite–magnetite as the interstitial phase between clinopyroxenes; (c, d) anhedral biotites and core–rim-zoned clinopyroxenes in gabbro; (e) intergrowth of ilmenite and magnetite in mineralized clinopyroxenite, and magnetites showing exsolution lamellae of spinel and enclosing ilmenite; and (f) magnetites enclosing ilmenite and interstitial to clinopyroxenes in gabbro. Mineral abbreviations: Clinopyroxene (Cpx), plagioclase (Pl), biotite (Bt), apatite (Ap), ilmenite (Ilm), and magnetite (Mag).

2. Geological background and sample descriptions

2.1. Geological background and the Tarim Large Igneous Province

The Tarim Craton is bounded by the Tianshan, Kunlun, and Altyn orogenic belts (Fig. 1a–b). Early Permian igneous rocks are widespread in the Tarim Craton and include basalt, rhyolite, diabase, mafic–ultramafic intrusions, and syenitic rocks (Li et al., 2014; Xu et al., 2014; Zhang et al., 2008, 2010). Except for those covered by the Taklamakan desert (Fig. 1b), the early Permian igneous rocks are exposed mostly in the areas of Keping, Bachu, and Piqiang around the northwestern and southwestern margins of the Tarim Craton (Wei et al., 2014; Zhang et al., 2008, 2010). On the basis of geophysical investigations and borehole data, it has been suggested that the basalts may extend over an area of 250,000 km^2 in the interior of the craton, with a thickness varying from ~200 to ~800 m (Xu et al., 2014 and references therein). The estimated volume of the Tarim basalts is ~150,000 km^3, which is comparable with that of the Emeishan LIP (Xiao et al., 2004 and references therein). Thus, Tarim early Permian intraplate magmatism is regarded as forming an LIP, the Tarim large igneous province or TLIP (Xu et al., 2014). The formation of the TLIP is likely related to mantle plume activity, a proposal that is supported by the existence of a kimberlite–flood-basalt assemblage, large-scale crustal uplift, picrite, radiating mafic dike swarms, large-scale Fe–Ti-oxide deposits, and high-temperature granites (Xu et al., 2014).

The TLIP has been subdivided into three magmatic episodes, namely, ca. 300 Ma small-volume kimberlitic rocks, ca. 290 Ma flood basalts, and ca. 280 Ma ultramafic–mafic–felsic intrusions and dike swarms (Xu et al., 2014). The ca. 290 Ma flood basalts are widespread across the province, whereas the ca. 300 Ma kimberlitic rocks and ca. 280 Ma ultramafic–mafic–felsic intrusions and dike swarms are confined to the Bachu Uplift and the margins of the Tarim Craton (Fig. 1; Xu et al., 2014).

The major ore resources in the TLIP are Fe–Ti-oxide deposits and Cu–Ni sulfide deposits (Qin et al., 2011; Xu et al., 2014). Cu–Ni sulfide deposits are mainly distributed in the East Tianshan and Beishan

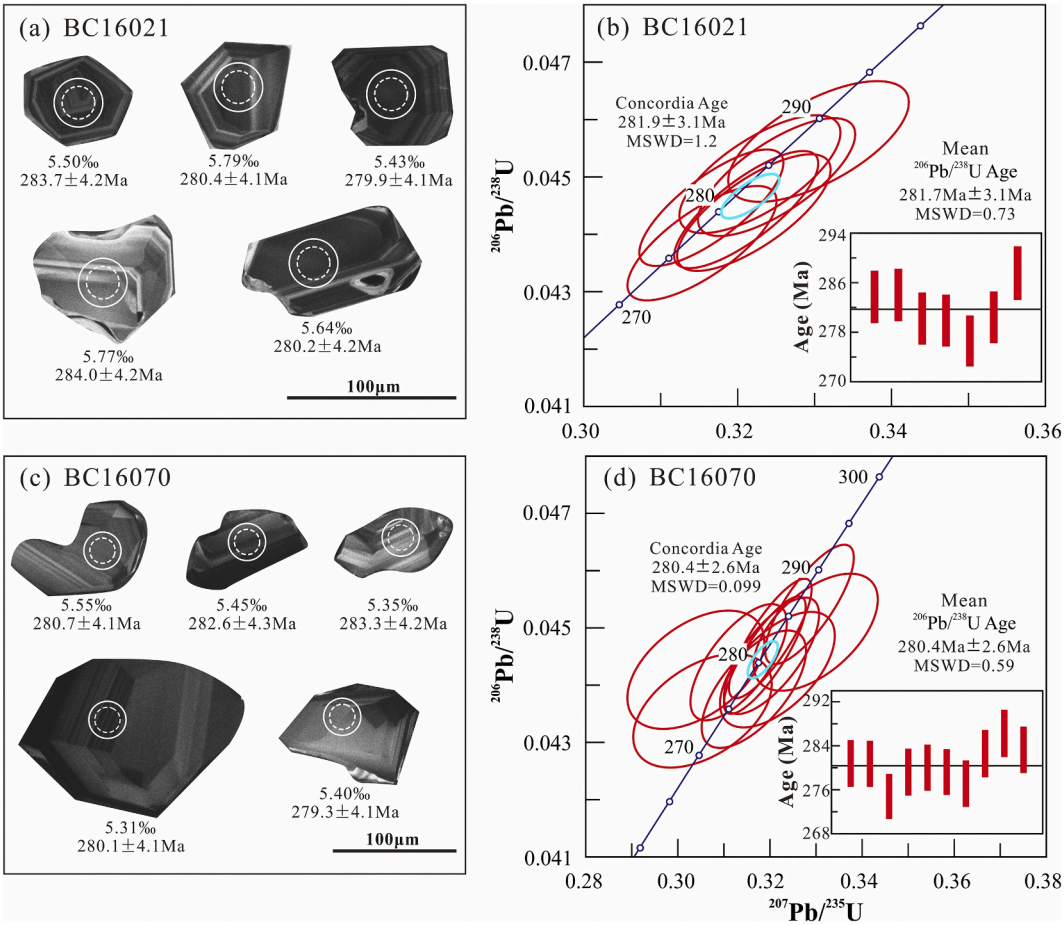

Fig. 3. Representative cathodoluminescence images of zircons and concordia diagrams of SIMS zircon U–Pb geochronology for Wajilitag gabbros. (a–b) Sample BC16021 and (c–d) sample BC16070. Dotted and solid circles show the locations of SIMS O isotope and U–Pb age analyses, respectively.

orogens (Qin et al., 2011), while Fe–Ti-oxide deposits are hosted by the layered mafic–ultramafic intrusions in the western margin of the Tarim Craton (e.g., Wajilitag, Mazhaertag and Piqiang intrusions at ~280 Ma; Cao et al., 2014, 2017; Wei et al., 2014; Zhang et al., 2016) and the Southwest Tianshan Orogen (e.g., Haladala intrusion at ~300 Ma; He et al., 2016). These layered mafic–ultramafic intrusions were interpreted as the magmatism of the Tarim mantle plume (Cao et al., 2014, 2017; He et al., 2016; Wei et al., 2014; Zhang et al., 2016).

2.2. Magmatism in the Wajilitag area

Abundant end-Carboniferous to early Permian magmatic rocks are found in the Wajilitag area of the northwestern margin of the Tarim Craton (Fig. 1c). The lithologies include kimberlitic rocks, clinopyroxenite, gabbro, diabase, syenitic rocks, diorite, nephelinite, and carbonatite (Cao et al., 2014, 2017; Cheng et al., 2015; Zhang et al., 2008; Zhang et al., 2013; Zhang et al., 2016, 2018; Zou et al., 2015). The Wajilitag kimberlitic rocks consist of multiple pipes and dike swarms, and baddeleyite and perovskite separated from kimberlitic samples show uniform concordia U–Pb ages of ca. 300 Ma (Zhang et al., 2013). The layered mafic–ultramafic intrusion consists of olivine clinopyroxenite (Ol = 10–20%), clinopyroxenite (Ol < 3%) and gabbro (Ol < 2%) from base upwards (Cao et al., 2014; Zhang et al., 2018), which are the main igneous rocks in the Wajilitag area. They show a gradual transition in lithology, have similar zircon U–Pb ages (284.2–281.3 Ma; Zhang et al., 2016; Cao et al., 2017), and are intruded into upper Devonian metamorphosed continental clastic sequences (Fig. 1c). The Wajilitag layered intrusion hosts a large-scale Fe–Ti-oxide deposit (Cao et al., 2014) that contains 146 million tons of ore reserves with ~17 wt% FeO^T, 7 wt% TiO_2, and 0.2 wt% V_2O_5 according to a report released in 2010 by the Xinjiang Bayi Iron & Steel Ltd. The Wajilitag Fe–Ti-oxide ore bodies occur as lenses or pods in the (olivine) clinopyroxenites, and disseminated ores have been mainly identified in the complex (Fig. 1c–d). The disseminated ores in the Wajilitag show transitional contacts with the adjacent silicate rocks and typically consist of 25–40% titanomagnetite, 10–15% ilmenite and 30–50% clinopyroxene with minor plagioclase and olivine (Zhang et al., 2018). Mafic dikes typically intrude the layered mafic–ultramafic intrusion or upper Devonian sedimentary rocks (Fig. 1c).

2.3. Petrography of the studied samples

The studied samples collected from the Wajilitag area consist of 3 clinopyroxenites, 7 gabbros, and 20 diabases.

Diabase samples show porphyritic texture with variable amounts of clinopyroxene phenocrysts (Fig. 2a). The groundmass shows ophitic texture and consists of plagioclase, clinopyroxene, Fe–Ti-oxides, biotite, hornblende, and apatite (Fig. 2a). Fine-grained clinopyroxenes and/or biotites are interstitial to plagioclases (Fig. 2a).

Clinopyroxenite samples were collected from the orebody and are composed of dominant clinopyroxene (70–80%) and Fe–Ti-oxides (20–30%; Fig. 2b) with minor hornblende and biotite (< 1%), which is termed as mineralized clinopyroxnite in this study. Clinopyroxene grains are usually euhedral to subhedral with a grain size of 0.3–1.5 mm (Fig. 2b). Gabbro samples show gabbroic texture and are composed of plagioclase (35–50%), clinopyroxene (35–45%), Fe–Ti-oxides (3–6%), and biotite (3–6%), with minor olivine (< 2%) and apatite (1–2%) (Fig. 2c–d). Some clinopyroxenes in gabbro samples show zoning texture

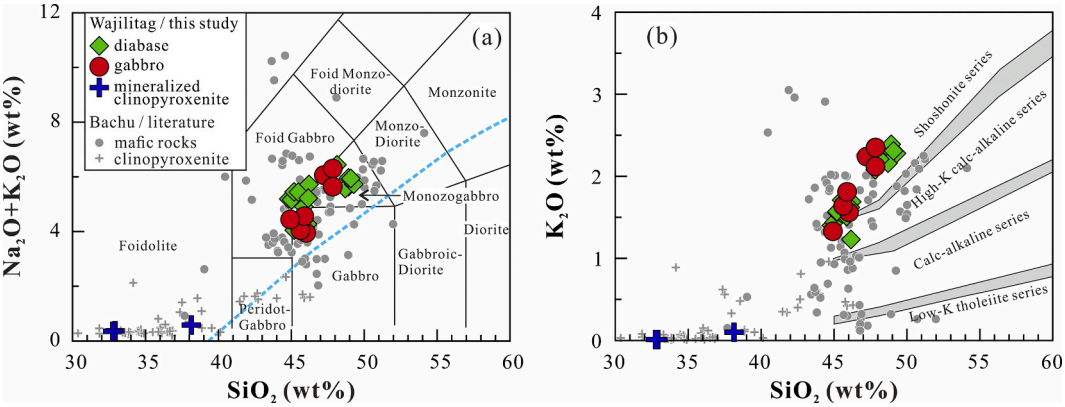

Fig. 4. (a) TAS (after Le Maitre et al., 1989) and (b) K_2O versus SiO_2 (after Middlemost, 1994) diagrams for Wajilitag mafic–ultramafic rocks. Data for early Permian clinopyroxenites and mafic rocks in the Bachu area are compiled in Supplementary Table 7.

with a euhedral core (Fig. 2c). Minor similar euhedral zoned clinopyroxenes also occur in mineralized clinopyroxenite samples. The Fe–Ti-oxides in mineralized clinopyroxenite and gabbro samples all consist of magnetite and ilmenite, which are generally interstitial to clinopyroxene and/or plagioclase (Fig. 2). Small amounts of fine-grained magnetites and ilmenites are wrapped in clinopyroxene (Fig. 2b). Magnetites typically contain spinel exsolution lamellae and enclose ilmenite in mineralized clinopyroxenite and gabbro samples (Fig. 2e–f).

3. Analytical methods

Whole-rock major element oxides were analyzed by X-ray fluorescence (XRF) at the ALS Chemex (Guangzhou) Co Ltd. Analytical precision is generally better than 2% for most oxides and better than 1% for SiO_2. The other analyses, including whole-rock trace elements and Sr–Nd–Hf isotopes, zircon U–Pb dating and O isotope, mineral composition and BSE images were carried out at the State Key Laboratory of Isotope Geochemistry, Guangzhou Institute of Geochemistry, Chinese Academy of Sciences (SKLaBIG-GIGCAS).

Whole-rock trace elements were analyzed by a Thermo iCAP Qc inductively-coupled plasma source mass spectrometer (ICP-MS). Powdered samples were dissolved in high-pressure Teflon bombs using a HF-HNO_3 mixture. Trace element concentrations were calibrated using USGS and Chinese National standards AGV-2, GSR-1, GSR-2, GSR-3, BHVO-2, W-2a, SY4 and SARM-4. Analytical precision of REE and other incompatible elements is typically 1–5%.

Whole-rock Sr–Nd–Hf isotopes were determined using a Finnigan Neptune multi-collector (MC)-ICP-MS, following the similar procedures described by He et al. (2016). Measured $^{87}Sr/^{86}Sr$, $^{143}Nd/^{144}Nd$ and $^{176}Hf/^{177}Hf$ ratios were normalized to $^{86}Sr/^{88}Sr = 0.1194$, $^{146}Nd/^{144}Nd = 0.7219$ and $^{179}Hf/^{177}Hf = 0.7325$, respectively. Reference standard BHVO-2 analyzed along with the unknowns gave $^{87}Sr/^{86}Sr = 0.703456 \pm 0.000028$ ($n = 10$; 2σ), $^{143}Nd/^{144}Nd = 0.512984 \pm 0.000011$ ($n = 8$; 2σ), and $^{176}Hf/^{177}Hf = 0.283095 \pm 0.000004$ ($n = 4$; 2σ), consistent with the recommended values ($^{87}Sr/^{86}Sr = 0.703481 \pm 0.000020$, $^{143}Nd/^{144}Nd = 0.512983 \pm 0.000010$, and $^{176}Hf/^{177}Hf = 0.283096 \pm 0.000020$, respectively; Weis et al., 2005).

Cathodoluminescence (CL) images of zircons were obtained using a Carl Zeiss SUPRA55SAPPHIRE Field Emission-Scanning Electron Microscopy (FE-SEM) to characterize the internal structures. The CL images of representative zircons are shown in Fig. 3.

In-situ zircon U–Pb ages and oxygen isotope were performed on a Cameca IMS-1280HR ion microprobe. The detailed analytical procedures are similar to those described by Li et al. (2010). For the O isotopic analyses, the $^{133}Cs^+$ primary ion beam was accelerated at 10 kV, with an intensity of about 2 nA and focused on an area of 10 μm on the sample surface. The size of analytical spots is about 20 μm in diameter (10 μm beam diameter + 10 μm raster). Oxygen isotopes were measured in multi-collector mode using two off-axis Faraday cups. The internal precision of a single analysis generally was better than 0.1‰ (1σ) for the $^{18}O/^{16}O$ ratio. The measured oxygen isotopic data were corrected for instrumental mass fractionation (IMF) using the Penglai zircon standard, which was analyzed once every five unknowns. Six measurements of the Qinghu zircon standard during the course of this study yielded a weighted mean of $\delta^{18}O_{VSMOW} = 5.36 \pm 0.28‰$ (2σ), which is consistent with the reported value of 5.40 ± 0.20‰ within errors (Li et al., 2013). For zircon U–Pb dating, the ellipsoidal spot is about 20 μm × 30 μm in size. Calibration of Pb/U ratios is relative to the standard zircon Plesovice, which was analyzed once every four unknowns. A long-term uncertainty of 1.5% (1 RSD) for $^{206}Pb/^{238}U$ measurements of the standard zircons was propagated to the unknowns (Li et al., 2010), despite that the measured $^{206}Pb/^{238}U$ error in a specific session is generally around 1% (1 RSD) or less. U and Th concentrations of unknowns were also calibrated relative to the standard zircon Plesovice. Measured compositions were corrected for common Pb using non-radiogenic ^{204}Pb. A secondary standard zircon Qinghu (Li et al., 2013) was analyzed as unknown to monitor the reliability of the whole procedure. Uncertainties on single analyses are reported at the 1σ level; mean ages for pooled U–Pb analyses are quoted with a 95% confidence interval.

Major elements compositions of clinopyroxene and olivine were carried out using the Cameca SXFive FE Electron Probe Microanalyzer (EPMA). The operating conditions are: 20 kV accelerating voltage, 20–40 nA beam current. A variable peak counting time of 8–180 s was used depending on the intensity of characteristic X-ray line. Calibration standards used for minerals analysis were silicate and oxide standards from SPI company.

Trace elements in clinopyroxene were measured with an ELEMENT XR (Thermo Fisher Scientific) ICP-SF-MS coupled with a 193-nm (ArF) Resonetics RESOlution M-50 laser ablation system. Laser condition was set as following: 24 μm beam size, 5 Hz repetition rate, ~4 J cm^{-2} energy density. A smoothing device (the Squid, Laurin Technic) was used to smooth the sample signal. Each spot analysis consisted of 20 s gas blank collection with the laser off, and 30 s sample signal detection with the laser on. The calibration line for each element was constructed by analyzing three USGS reference glasses BCR-2G, BHVO-2G and GSD-1G. The oxide molecular yield, indicated by the $^{232}Th^{16}O/^{232}Th$ ratio, was less than 0.3%. The detailed experiment procedure and data reduction strategy are described in Zhang et al. (2019). A USGS reference glass TB-1G was measured as unknown samples. Five analyses of TB-1G indicate most elements are within 8% of the reference values and the analytical precision (2RSD) was better than 10% for most elements.

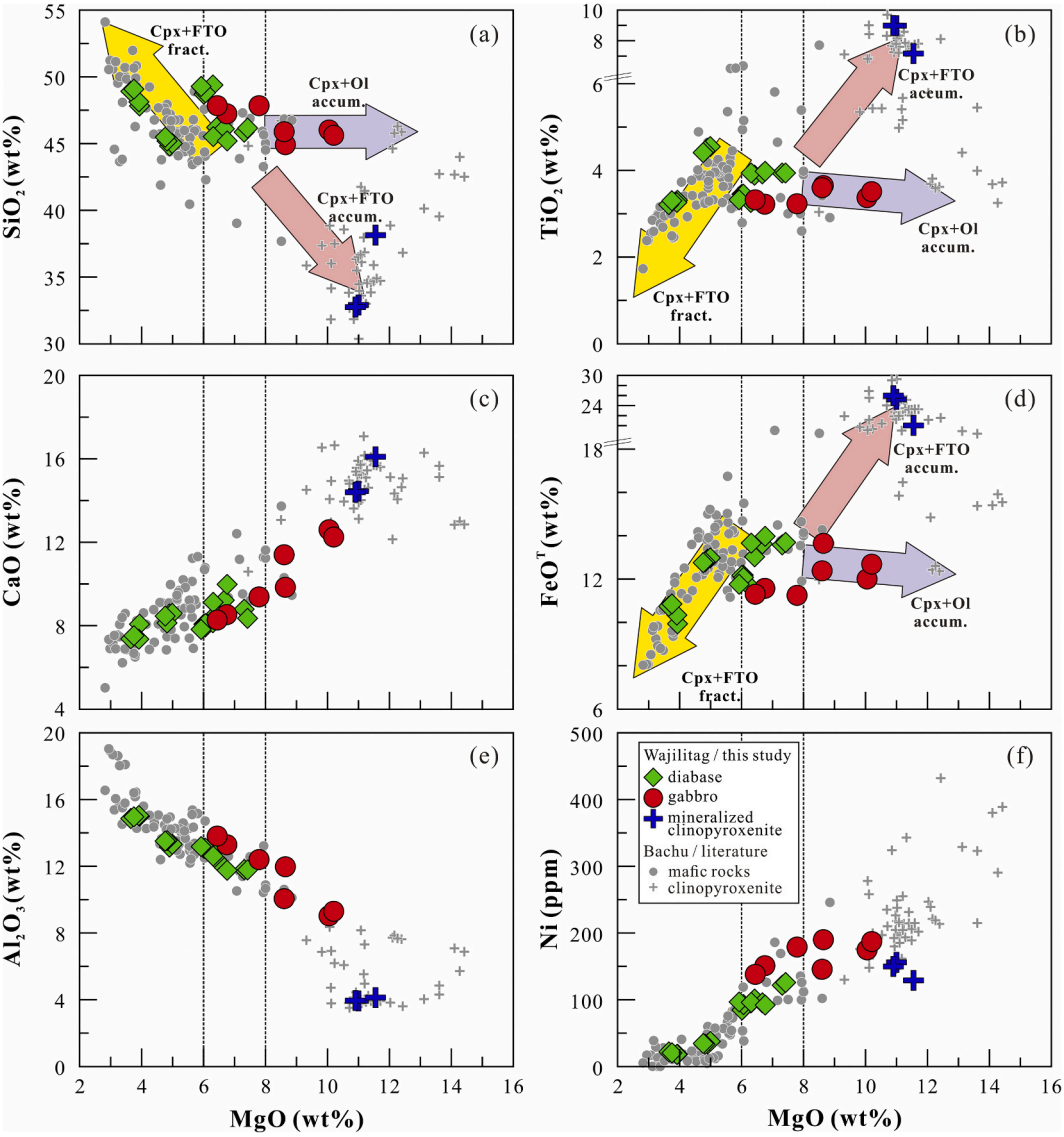

Fig. 5. Diagrams of representative major-element oxides (SiO_2, TiO_2, CaO, FeO^T, and Al_2O_3) (a–e) and Ni (f) versus MgO for Wajilitag mafic–ultramafic rocks. Data for early Permian clinopyroxenites and mafic rocks in the Bachu area are compiled in Supplementary Table 7.

4. Analytical results

Results for secondary ion mass spectrometry (SIMS) zircon U–Pb geochronology and O isotopes, as well as whole-rock major and trace elements, Sr–Nd–Hf isotopes, and mineral compositions, are given in Supplementary Tables 1–6, respectively.

4.1. In situ zircon U–Pb geochronology and O isotopes

Two gabbro samples were selected for zircon SIMS U–Pb dating and O isotope analyses (Supplementary Table 1). All zircons show well-developed oscillatory zoning in CL images (Fig. 3), indicating a magmatic origin.

Zircons from gabbro samples BC16021 and BC16070 have moderate Th and U contents (74–958 ppm and 81–347 ppm, respectively) with high Th/U ratios of 0.58–5.8 (Supplementary Table 1). The U–Pb results for sample BC16021 form a coherent cluster and yield a concordia age of 281.9 ± 3.1 Ma (MSWD = 1.2; n = 7) and a weighted mean $^{206}Pb/^{238}U$ age of 281.7 ± 3.1 Ma (MSWD = 0.73) (Fig. 3b). The U–Pb results for sample BC16070 also form a coherent cluster and yield a concordia age of 280.4 ± 2.6 Ma (MSWD = 0.1; n = 10) and a mean $^{206}Pb/^{238}U$ age of 280.4 ± 2.6 Ma (MSWD = 0.59; Fig. 3d), which are identical to the ages for sample BC16021 within errors and are interpreted as the emplacement age of the Wajilitag gabbros. These zircons have $\delta^{18}O$ values of 4.90‰–6.08‰ with mean values of 5.69‰ ± 0.31‰ (2SD) and 5.32‰ ± 0.40‰ (2SD) for samples BC16021 and BC16070, respectively.

4.2. Whole-rock major and trace elements

The studied samples have variable whole-rock major-element compositions (SiO_2 = 32.75–49.51 wt%, MgO = 3.65–11.55 wt%, FeO^T = 9.93–26.00 wt%, and CaO = 7.35–16.10 wt%; Figs. 4 and 5). The samples show overall high alkali contents, display alkaline affinities on a total-alkali–silica (TAS) diagram (Fig. 4a), and belong to the shoshonite series in a diagram of K_2O vs. SiO_2 (Fig. 4b). Mineralized clinopyroxenite samples have the highest MgO (10.90–11.55 wt%), FeO^T (20.04–26.00 wt%), TiO_2 (7.16–8.99 wt%), and CaO (14.40–16.10 wt%) and the lowest SiO_2 (32.75–38.14 wt%), Al_2O_3 (3.93–4.13 wt%) and alkali (0.35–0.58 wt%) contents (Figs. 4 and 5). Gabbro and diabase samples have variable MgO (3.65–10.20 wt%) with slightly variable SiO_2 (44.82–49.51 wt%), TiO_2 (3.21–4.55 wt%), and FeO^T contents (9.93–13.97 wt%). In the Harker diagrams, SiO_2 and Al_2O_3 contents

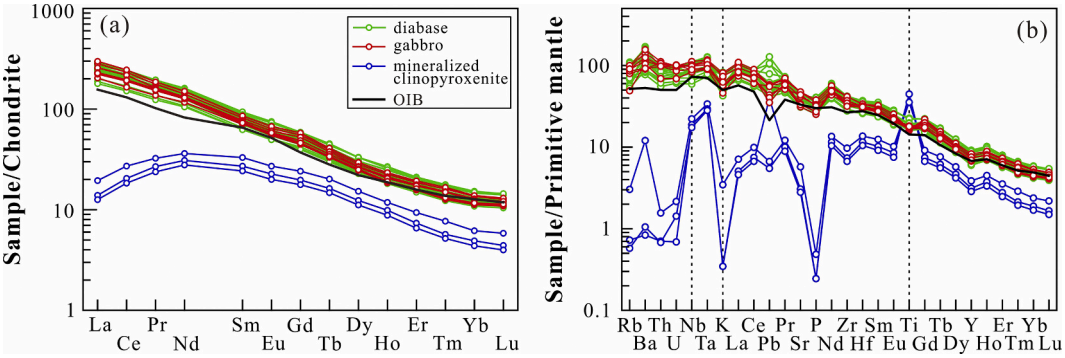

Fig. 6. (a) Chondrite-normalized REE patterns and (b) primitive-mantle-normalized trace-element variation diagrams for Wajilitag mafic–ultramafic rocks. Chondrite and OIB values are from Sun and McDonough (1989). Primitive-mantle values are from McDonough and Sun (1995).

increase gradually with decreasing MgO from mineralized clinopyroxenite through gabbro to diabase (Fig. 5a and e). There is a change in the trend of SiO_2, TiO_2, and FeO^T at MgO ≈ 5–6 wt% (Fig. 5a, b, and d).

The contents of compatible trace elements such as Ni, V, Co, Cr, and Sc of the studied samples are highly variable (18.0–191 ppm, 208–806 ppm, 24.7–97.9 ppm, 2.53–769 ppm, and 15.2–59.4 ppm, respectively). Gabbro and diabase samples have lower contents of these compatible trace elements, except for Cr, than mineralized clinopyroxenite samples (Supplementary Table 2 and Supplementary Fig. 1). Overall, the studied samples show strong positive correlations between these compatible trace elements (e.g., Ni; Fig. 5f) and MgO contents.

Mineralized clinopyroxenite samples display convex rare earth element (REE) patterns that have low La/Sm (0.79–0.91) and high Sm/Yb ratios (4.81–4.99) (Fig. 6a). The samples are depleted in large-ion lithophile elements (LILEs; e.g., Rb, Ba, Th, U, and K) and show positive Nb, Ta, and Ti anomalies in trace-element variation diagrams (Fig. 6b) owing to the accumulation of clinopyroxenes and Ti–Fe-oxides (Fig. 2b). Gabbro and diabase samples show similar REE patterns that are highly fractionated between light REEs (LREEs) and heavy REEs (HREEs) with high La/Yb ratios (22.9–30.9), resembling typical ocean island basalt (OIB; Fig. 6a). These samples are also similar to OIB in trace-element variation diagrams, showing enrichment in LILEs, Nb and Ta without pronounced negative Ti anomaly (Fig. 6b).

4.3. Whole-rock Sr–Nd–Hf isotopes

Mineralized clinopyroxenite and gabbro samples have similar initial $^{87}Sr/^{86}Sr$, $^{143}Nd/^{144}Nd$, and $^{176}Hf/^{177}Hf$ ratios that show narrow ranges (0.70430–0.70464, 0.51231–0.51241, and 0.28271–0.28274, respectively). All samples show positive $\varepsilon_{Nd}(t)$ (+0.70 to +2.64) and $\varepsilon_{Hf}(t)$ (+3.46 to +4.49) values (Supplementary Table 3). Diabase samples have slightly higher $^{87}Sr/^{86}Sr$ ratios (0.70457–0.70578) and a wider range of, but overall slightly lower, initial $^{143}Nd/^{144}Nd$ (0.51216–0.51238) and $^{176}Hf/^{177}Hf$ ratios (0.28261–0.28273) than those of the intrusive rocks, corresponding to slightly variable $\varepsilon_{Nd}(t)$ values (−2.27 to +1.92) and $\varepsilon_{Hf}(t)$ values (−0.06 to +4.39). In isotope diagrams of ε_{Nd} vs. $^{87}Sr/^{86}Sr$ and ε_{Hf} vs. ε_{Nd}, the Wajilitag samples all plot within the field of OIBs (Fig. 7). Gabbro and diabase samples define a linear array that departs slightly from the terrestrial array in the diagram of ε_{Hf} vs. ε_{Nd} (Fig. 7b).

4.4. Mineral compositions

4.4.1. Olivine

Olivines from gabbro samples show a wide range of Fo contents (63.3–84.8) and have variable MnO (0.19–1.06 wt%), NiO (0.038–0.36 wt%), and CaO (0.014–0.29 wt%) contents (Supplementary Table 4). Some olivines have lower CaO contents than those of typical magmatic olivine (CaO > 0.1 wt%; Foley et al., 2013) despite their variable Fo contents (65.4–84.8). Overall, Ni contents of olivines decrease with decreasing Fo, consistent with the trend of fractional crystallization of olivines in a magmatic system (Fig. 8a). High-Fo (82.8–84.8) olivines have high Ni contents with high Fe/Mn ratios and plot in the field of olivines from pyroxenite-derived magmas, resembling olivines in the ferropicrites (Fig. 8; Gibson, 2002).

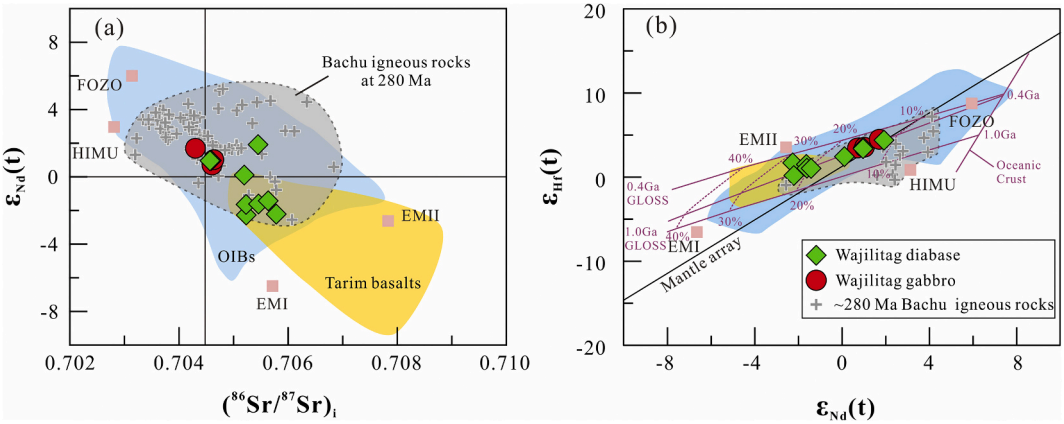

Fig. 7. Sr–Nd–Hf isotopes for Wajilitag mafic–ultramafic rocks. (a) $\varepsilon_{Nd}(t)$ versus $(^{86}Sr/^{87}Sr)_i$; and (b) $\varepsilon_{Hf}(t)$ versus $\varepsilon_{Nd}(t)$. $(^{86}Sr/^{87}Sr)_i$, $\varepsilon_{Nd}(t)$, and $\varepsilon_{Hf}(t)$ are all recalculated at 280 Ma. The Nd–Hf mantle array with the relationship described by $\varepsilon_{Hf} = 1.55\varepsilon_{Nd} + 1.21$ is from Vervoort et al. (2011). Data for FOZO, HIMU, EM1, and EM2 are from Stracke et al. (2003, 2005). Data for ~280 Ma igneous rocks in the Bachu area are compiled in Supplementary Table 7. Data for Tarim basalts are from the compilation by Li et al. (2014).

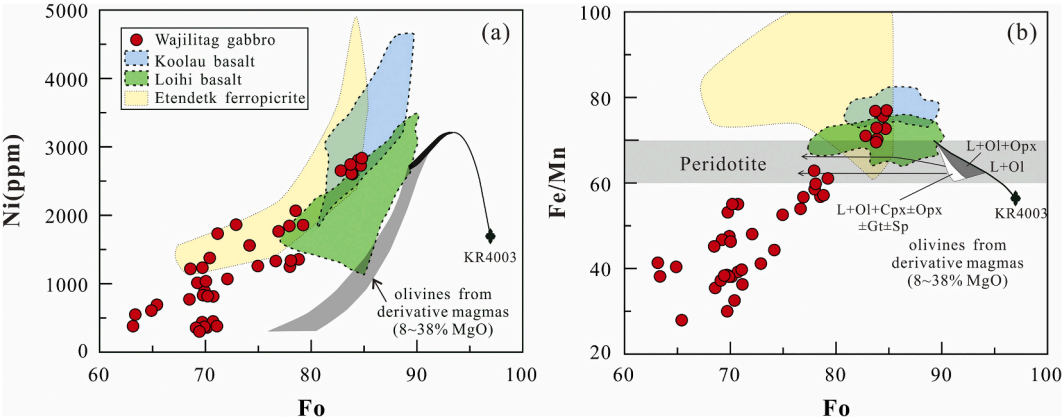

Fig. 8. Diagrams of Ni (a) and Fe/Mn (b) versus Fo for olivines from Wajilitag gabbros. Compositional fields of olivines from peridotite melts and Hawaii basalts (Koolau and Loihi) are from Herzberg (2011). The field of olivines from Etendetk ferropicrite is from Gibson et al. (2000) and Gibson (2002).

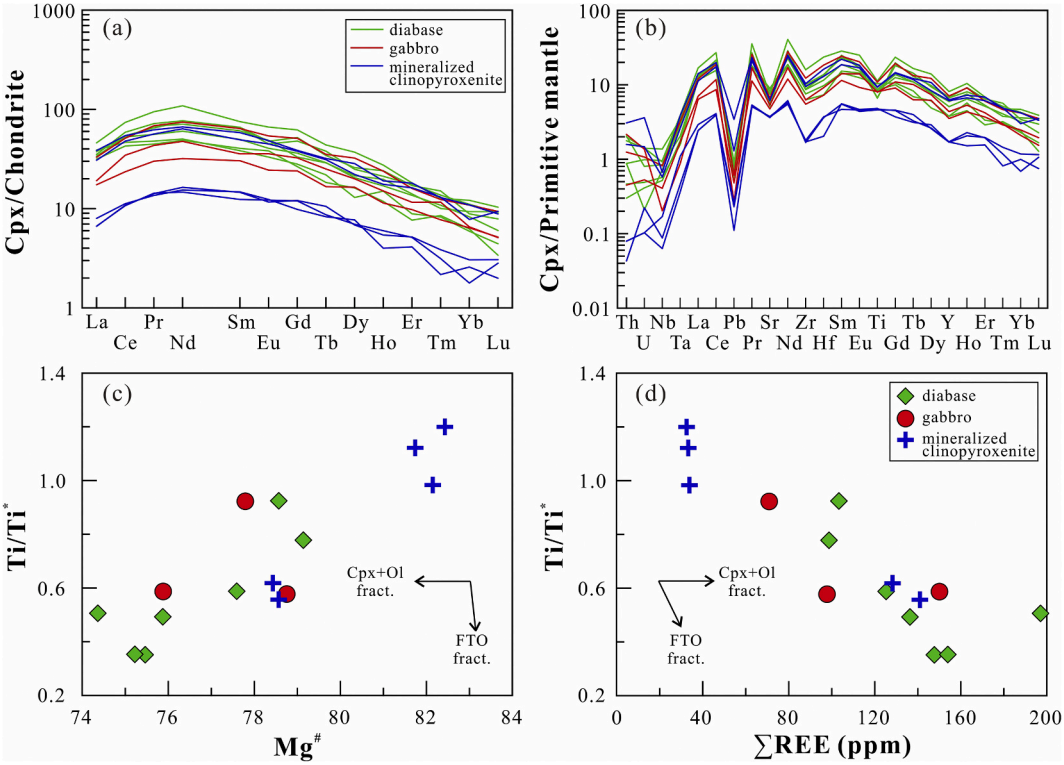

Fig. 9. (a) Chondrite-normalized REE patterns, (b) primitive-mantle-normalized trace-element variation diagrams, and plots of (c) $Mg^{\#}$ and (d) ∑REE versus Ti/Ti* for clinopyroxenes from Wajilitag mafic–ultramafic rocks. Chondrite values are from Sun and McDonough (1989), and primitive-mantle values are from McDonough and Sun (1995). $Ti/Ti^* = 2Ti_{PM}/(Sm_{PM} + Tb_{PM})$.

4.4.2. Clinopyroxene

Clinopyroxenes from mineralized clinopyroxenite, gabbro, and diabase samples have variable SiO_2 (46.37–52.72 wt%), MgO (12.28–17.19 wt%), FeO (5.12–9.44 wt%), CaO (20.04–22.61 wt%), TiO_2 (0.68–2.64 wt%), Al_2O_3 (1.52–6.38 wt%), Na_2O (0.34–0.93 wt%), MnO (0.08–0.33 wt%), and Cr_2O_3 (bdl.–0.84 wt%) contents and belong to Mg-augite or diopside with $Mg^{\#}$ values of 70.7–85.4 (Supplementary Table 5 and Supplementary Fig. 2). These clinopyroxenes show similar patterns of $Mg^{\#}$ variation (Supplementary Fig. 2), except for some low-$Mg^{\#}$ clinopyroxenes from gabbro samples, which have higher SiO_2 but lower TiO_2 contents than others at a given $Mg^{\#}$ owing to fractional crystallization of Ti–Fe-oxides, corresponding to slight negative Ti anomalies for some gabbro samples (Fig. 6d). All clinopyroxenes show a positive correlation between TiO_2 and Al^{IV} with similar Ti/Al ratios (0.20–0.35), similar to the trend of clinopyroxenes from rift-related mafic–ultramafic cumulates (Supplementary Fig. 2). In addition, all clinopyroxenes show parallel and convex-upward REE patterns (Fig. 9a) and display notably negative Pb and Sr anomalies on the trace elements patterns (Fig. 9b). Most of them exhibit negative Ti anomaly ($Ti/Ti^* < 1$), except for those with high $Mg^{\#}$ and low REE (Fig. 9c–d). Overall, Ti/Ti* values of these clinopyroxenes are positively correlated with $Mg^{\#}$ but negatively correlated with REE (Fig. 9c–d).

5. Discussion

5.1. Petrogenesis of the Wajilitag mafic–ultramafic rocks

5.1.1. Timing of emplacement of the Wajilitag mafic rocks

Zircon SIMS U–Pb dating results for two gabbro samples (281.9 ± 3.1 and 280.4 ± 2.6 Ma) of this study are consistent with previous dating results for gabbro and clinopyroxenite (284.2–281.3 Ma; Zhang et al., 2016; Cao et al., 2017) within errors, and all of these ages are close to the emplacement age of Xiaohaizi gabbro and diabase (Wei et al., 2014 and references therein) in the northwestern Wajilitag area (Fig. 1b). Although mafic dikes are intruded into gabbro and clinopyroxenite (Fig. 1c; Cao et al., 2014), zircon U–Pb dating of a Wajilitag alkali mafic dike has yielded an age of 281.4 ± 1.7 Ma (Zou et al., 2015), which is also identical to the emplacement age of intrusive rocks, within errors. Therefore, geochronological data show that gabbro, clinopyroxenite, and mafic dikes were emplaced almost simultaneously (at ca. 280 Ma) and belong to the final magmatic phase of the TLIP.

5.1.2. Alteration and crustal contamination

Several diabase samples have slightly higher LOI values (1.5%–2.5%) than those of other samples, as well as some secondary minerals, indicating some degree of alteration. Other samples are relatively fresh with low LOI values (<1.5%) and rarely have secondary minerals (Fig. 2), excluding the possibility of marked alteration. As Zr is stable during alteration and weathering, correlations between Zr and other elements can be used to determine whether these elements have been affected by alteration. The diabase, gabbro, and mineralized clinopyroxenite samples all show positive correlations between Zr and other trace elements (including REEs, HFSEs, and LILEs; Supplementary Fig. 1), suggesting that their trace-element contents are essentially unaffected by alteration.

Crustal contamination is inevitable for basaltic melts during their ascent through crust and their evolution within magma chambers in a continental crust environment. The $\varepsilon_{Nd}(t)$ values of Wajilitag mafic rocks are weakly correlated with SiO_2 and MgO contents, indicating slight crustal contamination (Supplementary Fig. 3). However, the level of crustal contamination is very low because the studied samples show OIB-like trace-element patterns (Fig. 6b) and have much higher Nb/U (34.2 ± 5.7; Supplementary Table 2) and lower Th/Nb (0.11 ± 0.03; Supplementary Table 2) ratios relative to continental crust (Nb/U = 4.44, Th/Nb = 0.70; Rudnick and Gao, 2003). In addition, the gabbro samples show mantle-derived zircon $\delta^{18}O$ values (4.90‰–6.08‰; Supplementary Table 1), further indicating that crustal contamination, if present, is negligible.

5.1.3. Fractional crystallization and accumulation

The Wajilitag gabbros and diabases are coeval and have similar trace-element and Sr–Nd–Hf isotopic compositions (Figs. 6 and 7), indicating similar mantle sources. In addition, clinopyroxenes from gabbro, diabase, and mineralized clinopyroxenite samples show the same major-elements compositional trends (Supplementary Fig. 2) and have similar Al/Ti ratios (0.20–0.35; Supplementary Table 5) with parallel trace elements patterns (Fig. 9c–d), demonstrating that these mafic–ultramafic rocks and associated ore deposits were derived from a common magma. As crustal contamination has a negligible effect on the compositional variation of Wajilitag mafic–ultramafic rocks, the wide range of major-element contents of these rocks should be related mostly to partial melting of their mantle sources and subsequent fractional crystallization and/or accumulation (Figs. 5, 9c–d).

MgO contents of the studied samples are negatively correlated with Al_2O_3 but positively correlated with CaO and Ni (Fig. 5), suggesting fractional crystallization or accumulation of mafic phases such as clinopyroxene and olivine. The change in trend of SiO_2, TiO_2, and FeO^T contents at MgO ≈ 5–6 wt% (Fig. 5a, b, and d) indicates a change in fractional crystallization or accumulation phases. For the diabase samples at MgO < 6 wt%, TiO_2 and FeO^T decrease and SiO_2 increases with decreasing MgO, corresponding to fractionation of Fe–Ti-oxides (Fig. 5a, b, and d). For the gabbro samples at MgO > 8 wt%, CaO increases steeply as MgO increases, indicative of clinopyroxene accumulation (Figs. 2c–d and 5c). Furthermore, the mineralized clinopyroxenite samples have the highest MgO, Al_2O_3, CaO, FeO^T, and TiO_2 and the lowest SiO_2, Na_2O, and K_2O contents as the result of the accumulation of clinopyroxene and Fe–Ti-oxides (Figs. 4 and 5).

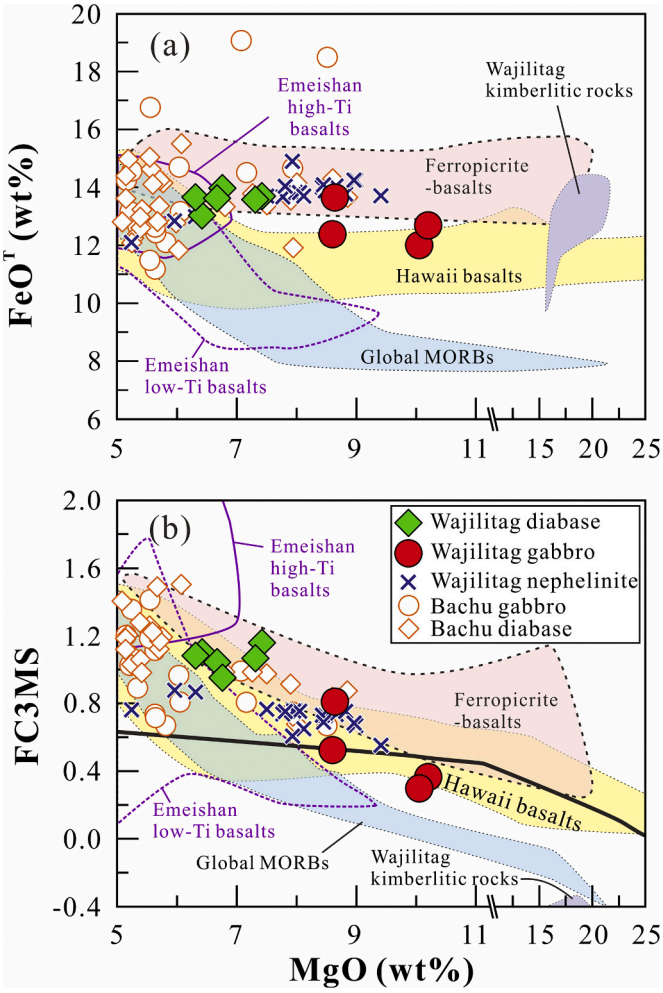

Fig. 10. Diagrams of FeO^T (a) and FC3MS (b) versus MgO for Wajilitag mafic rocks. The samples include diabases and gabbros that have not experienced significant Fe–Ti-oxides fractionation. Data for early Permian mafic rocks in the Bachu area are compiled in Supplementary Table 7. Literature data: global MORBs, including those from central India, southwest India, southeast India, the Atlantic, and the east Pacific mid-ridge, are from the PetDB database; Hawaii basalts are from GEOROC; Emeishan high-Ti and low-Ti basalts are from Xiao et al. (2004); ferropicrites and associated high-Fe basalts are from Hanski and Smolkin (1995), Gibson et al. (2000) and Gibson (2002); Wajilitag nephelinites are from Cheng et al. (2015), and Wajilitag kimberlitic rocks are from Zhang et al. (2013). The FC3MS boundary (bold black line) between peridotite-derived melts and pyroxenite melts is from Yang et al. (2016).

5.1.4. Magma source

The Tarim Craton has a relatively thick lithosphere of > 140 km at present (An and Shi, 2006) and might have been even thicker during the Permian (Wei et al., 2014; Xu et al., 2014). Because a thick lithosphere (> 130 km) will impede the upwelling of a mantle plume and thus prevent decompression melting of convective mantle (Sleep et al., 2002), some mafic rocks in the LIPs might have been derived from a subcontinental lithospheric mantle source (e.g., Xiao et al., 2004; Xu

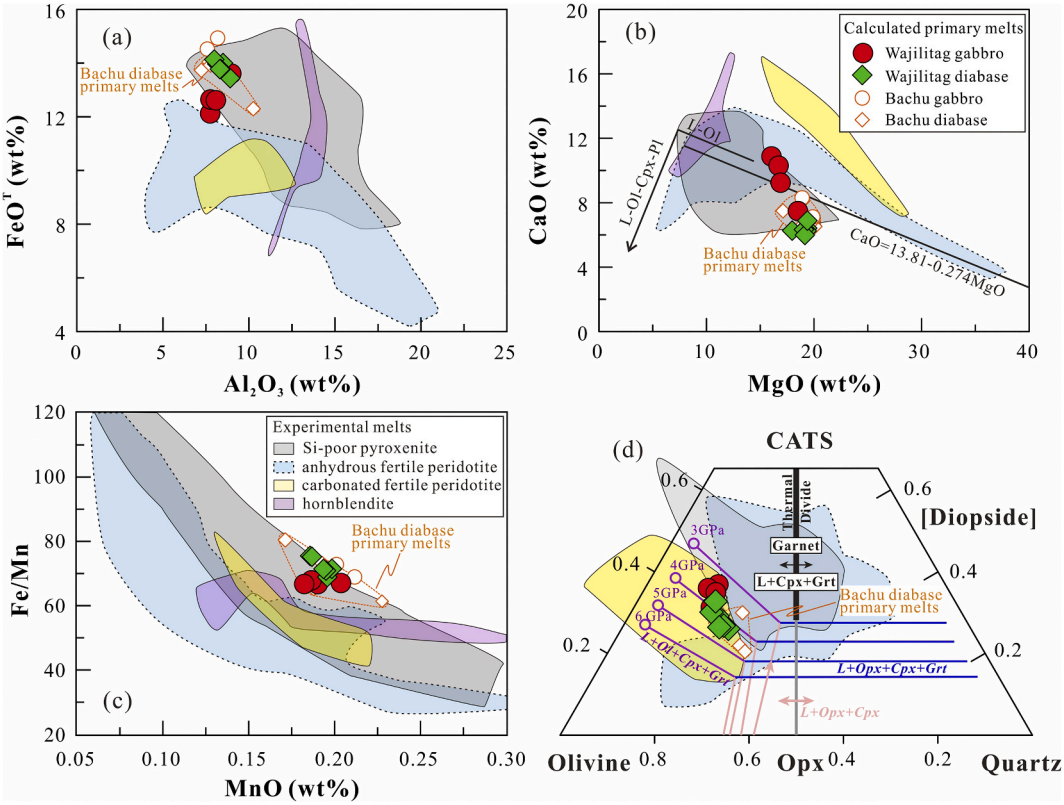

Fig. 11. Comparison of the calculated primary magma of Wajilitag mafic rocks with experimental partial melts. (a) FeO^T versus Al_2O_3; (b) CaO versus MgO; and (c) Fe/Mn versus MnO. Mafic rock samples include diabases and gabbros that have not experienced significant Fe–Ti-oxide fractionation (Ti/Ti* = 0.80–1.20) with MgO > 6 wt% . The primary magma compositions were calculated by adding equilibrium olivine until the melt were in equilibrium with olivine of Fo_{90} at QFM and 5 kb, using the program petrolog_v3.1.1.3 (see details in Supplementary Table 8). (d) Projections of calculated primary magma compositions from or towards diopside into the plane of olivine–quartz–calcium Tschermak's (CATS). The cotectics of [L + Opx + Cpx + Gt] and [L + Ol + Cpx + Gt] are from Herzberg (2011). Data for partial melts of anhydrous fertile peridotite (0.5–14 GPa), carbonated fertile peridotite (3 GPa), Si-poor pyroxenite/eclogite (2.0–5.0 GPa), and hornblendite (1.5 GPa) are compiled in Supplementary Table 9.

et al., 2014). Indeed, the Tarim flood basalts at ca. 290 Ma have alkaline affinity, with pronounced negative Nb and Ta anomalies in primitive-mantle-normalized trace-element patterns (Wei et al., 2014) and mostly negative $\varepsilon_{Nd}(t)$ values (−9.15 to +0.23; Fig. 7a; Wei et al., 2014), indicating a subduction-metasomatized subcontinental lithospheric mantle source (Wei et al., 2014; Xu et al., 2014). However, most of the Wajilitag mafic rocks have depleted Sr–Nd–Hf isotopes (Fig. 7) and OIB-like trace-element patterns that display enrichment in LREEs, Rb, Ba, Th, and U, and positive Nb and Ta anomalies and negative Pb and K anomalies (Fig. 6b), indicating their affinity to an asthenospheric mantle source.

5.2. Genesis of Fe-rich magma: partial melting of si-poor pyroxenite/eclogite

Mafic–ultramafic rocks in the TLIP, such as kimberlitic rocks, nephelinite, and diabase, have overall high FeO^T contents (Cao et al., 2014; Cheng et al., 2015; Zhang et al., 2010, 2013, 2018) compared with global MORBs and Emeishan low-Ti basalts (Fig. 10a). Specifically, the Wajilitag kimberlitic rocks with MgO > 20 wt% contain much higher FeO^T (12.5–14.1 wt%; Fig. 10a; Zhang et al., 2013) than global kimberlites (mostly 5–11 wt%; Canil and Bellis, 2007). Overall, the FeO^T contents of Wajilitag mafic rocks without significant fractionation of Fe–Ti-oxides (Ti/Ti* > 0.80) are similar to those of Emeishan high-Ti basalts and Hawaii basaltic rocks associated with mantle plumes (Fig. 10a).

Fe-rich melts can be generated by several processes: (a) liquid immiscibility of a differentiated basaltic magma (Charlier et al., 2011); (b) early-stage fractional crystallization of plagioclase from picritic/basaltic melt in a deeper magma chamber (Toplis and Carroll, 1995); (c) low-degree partial melting of peridotite at high pressure (Walter, 1998) or of carbonated peridotite (Davis et al., 2011); and (d) input of Fe-rich components, such as pyroxenite/eclogite or hornblendite, into the mantle source (Gibson, 2002; Gibson et al., 2000; Pilet et al., 2008; Tuff et al., 2005). Wajilitag mineralized clinopyroxenite samples have extremely low P_2O_5 contents (≤ 0.01 wt%; Supplementary Table 2), and the gabbro and diabase samples contain high alkali contents ($Na_2O + K_2O$ = 3.95–6.44 wt%; Fig. 4a), all of which differ from those of Fe-rich melts formed by liquid immiscibility, which generally have high P_2O_5 and low alkali contents (Charlier et al., 2011). Moreover, Wajilitag mafic rocks and coeval syenitic rocks in the Bachu area all plot away from the field of immiscibility liquid (Supplementary Fig. 4). Accordingly, there is no evidence to support liquid immiscibility in Wajilitag mafic–ultramafic rocks.

Fractional crystallization of Fe-poor minerals (e.g., plagioclase) in a deeper magma chamber can produce an Fe-rich residual magma (Toplis and Carroll, 1995), which is a common phenomenon for anhydrous magma. However, petrographic and major-element characteristics of Wajilitag mafic–ultramafic rocks clearly show that plagioclase was a late-stage phase (Figs. 2a–d and 5). The samples with relatively high MgO (> 6 wt%) and FeO^T (> 12 wt%) contain no plagioclase phenocrysts and have negligible Eu anomalies (Eu/Eu* = 0.97–1.01), which precludes early-stage fractional crystallization of plagioclase. In addition, accumulation of Fe–Ti-oxides in the early-stage can also increase FeO^T content of cumulate rocks significantly. However, both the whole-rocks and clinopyroxenes of Wajilitag diabase and gabbro samples show

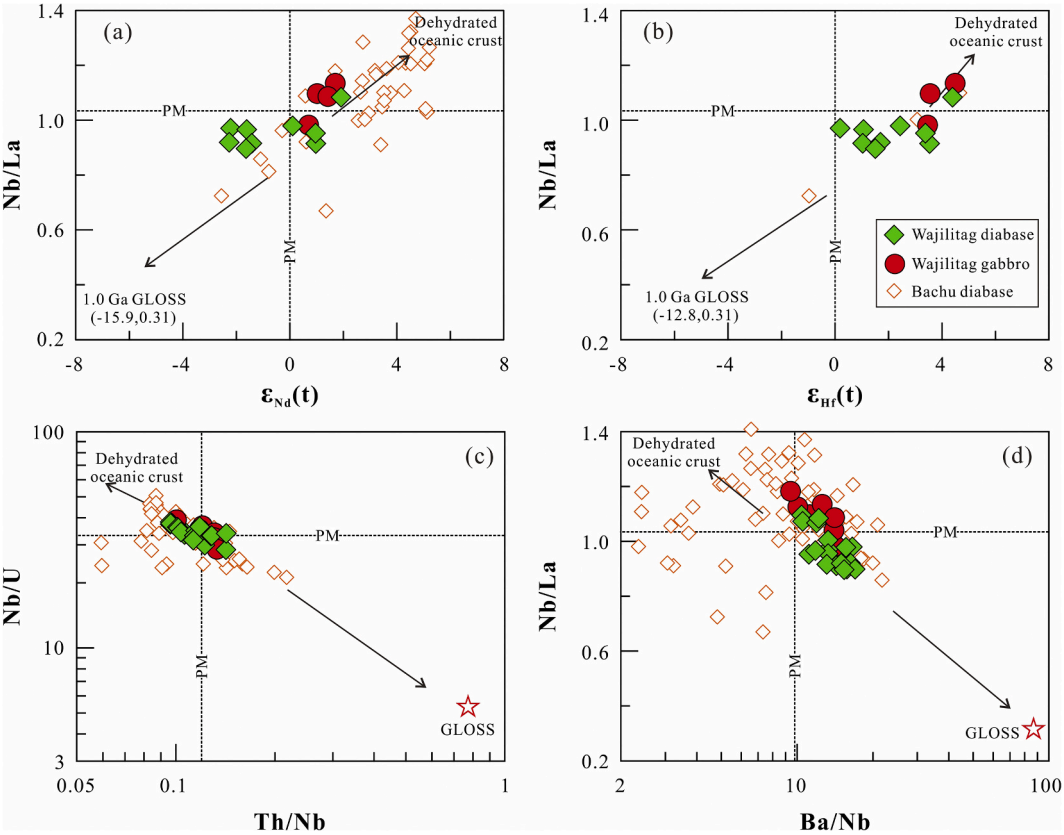

Fig. 12. Plots of (a) Nb/La versus $\varepsilon_{Nd}(t)$, (b) Nb/La versus $\varepsilon_{Hf}(t)$, (c) Nb/U versus Th/Nb, and (d) Nb/La versus Ba/Nb for Wajilitag mafic rocks. The average composition of global GLOSS is from Plank and Langmuir (1998). Data for early Permian diabases in the Bachu area are compiled in Supplementary Table 7.

insignificant or negative Ti anomaly (Figs. 6b, 9b), which excludes noticeable accumulation of Fe–Ti-oxides in the mafic rocks. On the other hand, the primary magma for Wajilitag diabases should have 13.0–14.1 wt% FeO^T and 18.0–19.4 wt% MgO according to the calculated melts in equilibrium with olivine of Fo_{90} (Supplementary Table 8; Fig. 11a), which is Fe rich and comparable with global Proterozoic–Phanerozoic ferropicrite (FeO^T = 12.5–15.8 wt%; MgO = 12.0–20.0 wt%; Hanski and Smolkin, 1995; Gibson et al., 2000; Gibson, 2002).

Low-degree partial melting of peridotite at high pressure or partial melting of carbonated peridotite and hornblendite can also produce Fe-rich primary magma (Dasgupta et al., 2007; Davis et al., 2011; Pilet et al., 2008; Walter, 1998). Wajilitag diabases have higher FC3MS ($FeO^T/CaO - 3MgO/SiO_2$) values than those of peridotite-derived melts (Fig. 10b), which excludes a source lithology of peridotite (Yang et al., 2016). In general, Al_2O_3 contents of peridotite-derived melts decrease with increasing pressure (Walter, 1998). This relationship can be applied to give an approximate estimate of the partial-melting depth of a peridotite source. For example, peridotite-derived melt might have a low Al_2O_3 content corresponding to high-pressure melting (Supplementary Table 9). The primary magma of Wajilitag diabases have lower Al_2O_3 (~8.0 wt%) and higher FeO^T relative to melts derived from fertile peridotite at a given Al_2O_3 content (Fig. 11a), indicating that low-degree partial melting of a peridotite source at high pressure cannot account for the Fe-rich characteristics of Wajilitag mafic rocks. For a carbonated peridotite source, at least 5–10 wt% CO_2 is required to produce a basaltic melt with 11.5–13.5 wt% FeO^T (Davis et al., 2011), which is a similar FeO^T content to that inferred for the Wajilitag primary magma. However, carbonated peridotite-derived melts would have much higher CaO contents than that inferred for the Wajilitag primary magma (Fig. 11b). In addition, such melts may show much lower FC3MS values (less than −0.3; Supplementary Table 9; Dasgupta et al., 2007) than those of Wajilitag diabase (FC3MS = 0.73–1.02; Supplementary Table 8), even though the source contains only 2.5 wt% CO_2 (Dasgupta et al., 2007). The (clinopyroxene) hornblendite-derived melts show much higher Al_2O_3 and CaO contents and lower Fe/Mn ratios relative to the inferred Wajilitag primary magma (Fig. 11a–c), indicating that hornblendite cannot be a suitable candidate for the mantle source of Fe-rich magma in the Wajilitag area.

Therefore, the Fe-rich characteristic of the Wajilitag primary magma can be attributed to partial melting of a mantle source enriched in eclogite or pyroxenite. Because clinopyroxene has lower partition coefficient ratios between Fe and Mn (D_{Fe}/D_{Mn}) compared with olivine (Foley et al., 2013), pyroxenite-derived melts should show higher Fe/Mn ratios relative to peridotite-derived melts at a given MnO content. Therefore, the primary magma of Wajilitag mafic rocks shows higher Fe/Mn ratios than those of (carbonated) peridotite- and hornblendite-derived melts, corresponding to partial melting of a mantle source enriched in eclogite/pyroxenite (Fig. 11c). Relatively primitive olivines (Fo = ~85 mol%) in Wajilitag mafic rocks have higher Ni contents and Fe/Mn ratios than those from MORBs, but are similar to those from Hawaii basalts (Fig. 8), which also indicates a mantle source enriched in eclogite/pyroxenite. Furthermore, because the melts derived from Si-rich eclogite/pyroxenite have much higher SiO_2 (> 48 wt%; Herzberg, 2011; Lambart et al., 2013 and references therein) relative to Wajilitag primary magma (SiO_2 < 46 wt%; Supplementary Table 8), Si-poor eclogite/pyroxenite could be the best candidate for the source lithology of Wajilitag mafic rocks. On an olivine–quartz–calcium Tschermak's (CATS) projection from or towards diopside (Herzberg, 2011), the inferred Wajilitag primary magma clearly plots on the Si-poor side and along the cotectic line of "L + Ol + Cpx + Gt" at ~4 GPa (Fig. 11d), corresponding to a mantle source enriched in Si-poor pyroxenite/eclogite.

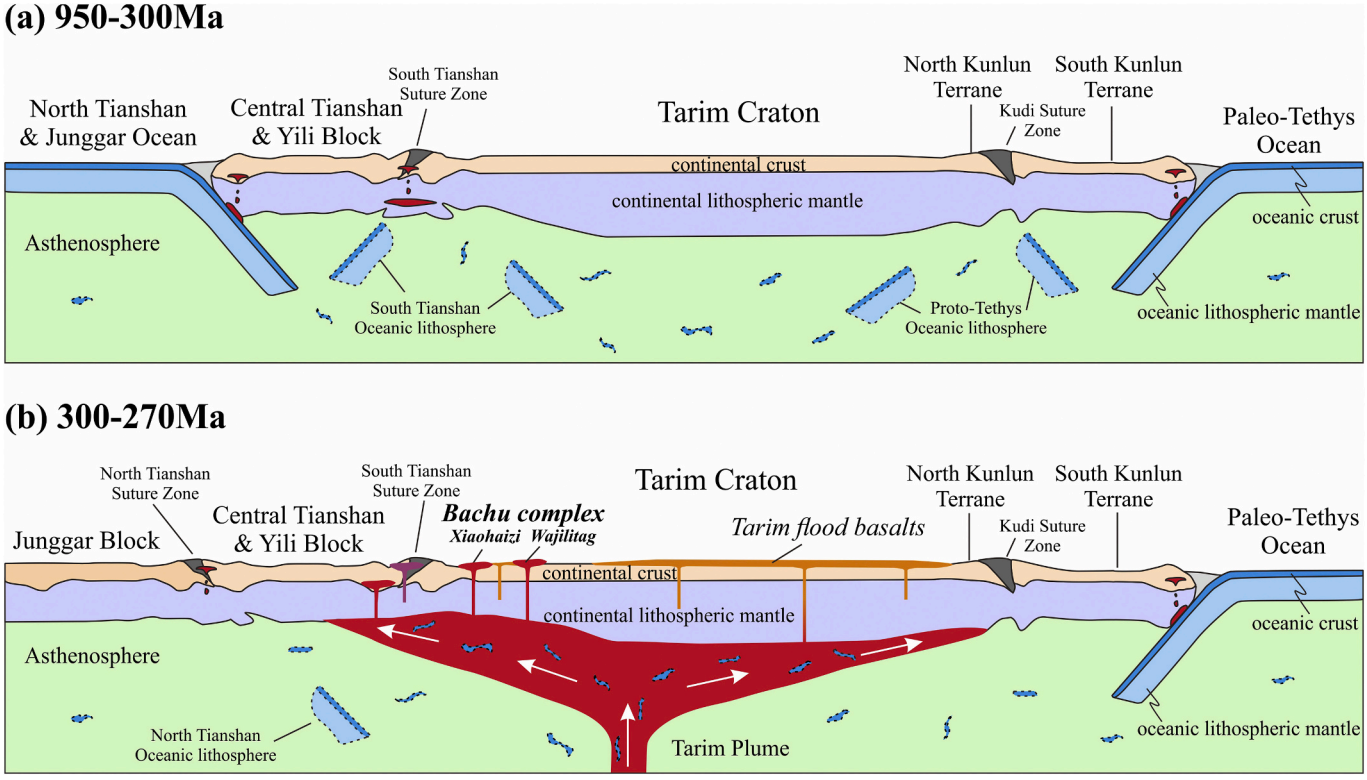

Fig. 13. Schematic model illustrating the generation of Wajilitag Fe-rich igneous rocks. (a) Long-term accretionary orogenesis in the northern (Tianshan Orogen) and southern (Kunlun Orogen) margins of the Tarim Craton. Accretionary orogenic history of the Tianshan Orogen: at 980–600 Ma, Paleo-Asian oceanic lithosphere subducted beneath the Tarim Craton and eventually resulted in the opening of the South Tianshan Ocean as a back-arc basin at 600 Ma (Ge et al., 2014); at 460–400 Ma, bidirectional subduction beneath the South Tianshan Ocean formed the Yili–Central Tianshan–Hanshan arcs in the north and the northern Tarim arc in the south, and the South Tianshan Ocean closed during the late Carboniferous (Ge et al., 2014; Zhong et al., 2019). Accretionary orogenic history of the West Kunlun Orogen: Proto-Tethys oceanic plate subducted beneath the South Kunlun Terrane and North Kunlun Terrane (Tarim) in the late Cambrian–Ordovician, followed by closure of the Proto-Tethys Ocean at 455–400 Ma (Wang et al., 2020); Paleo-Tethys oceanic plate subducted beneath the Kunlun Terrane (Tarim) from the early Carboniferous to late Triassic (Xiao et al., 2005). Subducted slabs can remain in the upper mantle for over 100 Myr (Richter et al., 2020) and can be transformed into Si-poor or Si-rich pyroxenites at upper-mantle depths (Herzberg, 2011; Lambart et al., 2013). (b) Hot and buoyant mantle plume carrying Si-poor pyroxenite (recycled oceanic crust) upwelled and ponded in the bottom of the lithosphere beneath the Tarim Craton. Owing to conductive heating by the Tarim mantle plume, partial melting of enriched metasomatized subcontinental lithosphereic mantle with or without plume materials produced Tarim flood basalts (Li et al., 2014; Xu et al., 2014). Partial melting of a mantle plume with Si-poor pyroxenite at the margin of the Tarim Craton formed the Wajilitag mainly Fe-rich mafic rocks and large-scale Fe–Ti-oxide deposits.

5.3. Involvement of recycled oceanic crust in the mantle source

During the subduction and subsequent dehydration of oceanic crust, fluid-mobile elements (e.g., Ba, K, Sr, Pb, Th, and U) are lost, whereas fluid-immobile elements (e.g., Nb and Ta) are preferentially retained in the residual slab (Kessel et al., 2005). Therefore, dehydrated oceanic crust should show negative Sr, K, and Pb anomalies, as well as low Th/Nb and high Nb/La and Nb/U ratios. Most of the Wajilitag mafic rocks show negative Sr, K, and Pb anomalies (Fig. 6b), and some samples, especially those with depleted Nd and Hf isotopes, have lower Th/Nb but higher Nb/La and Nb/U ratios than those of the primary mantle (Fig. 12), consistent with the involvement of dehydrated oceanic crust in their mantle source. This is also supported by the mantle-like zircon $\delta^{18}O$ values of Wajilitag mafic rocks (Supplementary Table 1). In contrast, Wajilitag mafic rocks have variable Nd–Hf isotopic compositions that define a linear array that departs slightly from the terrestrial array but plots on the mixing curve between recycled oceanic crust and sediments at 0.4–1.0 Ga (Fig. 7b). The involvement of recycled sediments in a mantle source would induce higher Ba/Nb and Th/Nb but lower Nb/La, Nb/U, $^{143}Nd/^{144}Nd$, and $^{176}Hf/^{177}Hf$ ratios in the melt, as such sediments are enriched in Ba, Th, and La relative to Nb and usually have enriched Nd–Hf isotopic compositions (Plank and Langmuir, 1998). Therefore, positive correlations of Nb/La with $\varepsilon_{Nd}(t)$ and $\varepsilon_{Hf}(t)$, and negative correlations of Nb/La with Ba/Nb, Nb/U, and Th/Nb in the Wajilitag mafic rocks (Fig. 12), in addition to the linear array of Nd–Hf isotopic compositions, clearly point to the involvement of recycled oceanic crust and sediments in the mantle source. The key issue is how and when these materials were recycled into the mantle source.

The northern margin of the Tarim Craton was strongly influenced by southward subduction during the Neoproterozoic and Paleozoic (950–300 Ma; Ge et al., 2014; Zhong et al., 2019). Moreover, the southern margin of the Tarim Craton and the West Kunlun region were continuously affected by northward subduction of Proto- and Paleo-Tethys oceanic lithosphere from the late early Paleozoic to early Mesozoic (i.e., 471–215 Ma), which formed abundant ophiolites and arc-related volcanic rocks in these areas (Wang et al., 2020; Xiao et al., 2005). Therefore, Neoproterozoic to Paleozoic subduction processes in the areas surrounding the Tarim Craton might have allowed input of oceanic crust and sediments into the asthenosphere under the marginal parts of the craton (Fig. 13).

5.4. Implications for the metallogenesis of Fe–Ti-oxide deposits in LIPs

Numerous studies have proposed that magmatic evolution is important to the generation of Fe–Ti-oxide deposits (Charlier et al., 2011; Namur et al., 2010; Song et al., 2013; Tang et al., 2021; Toplis and Carroll, 1995). However, the involvement of recycled oceanic crust in the mantle source may account for the genesis of Fe-rich primary magma

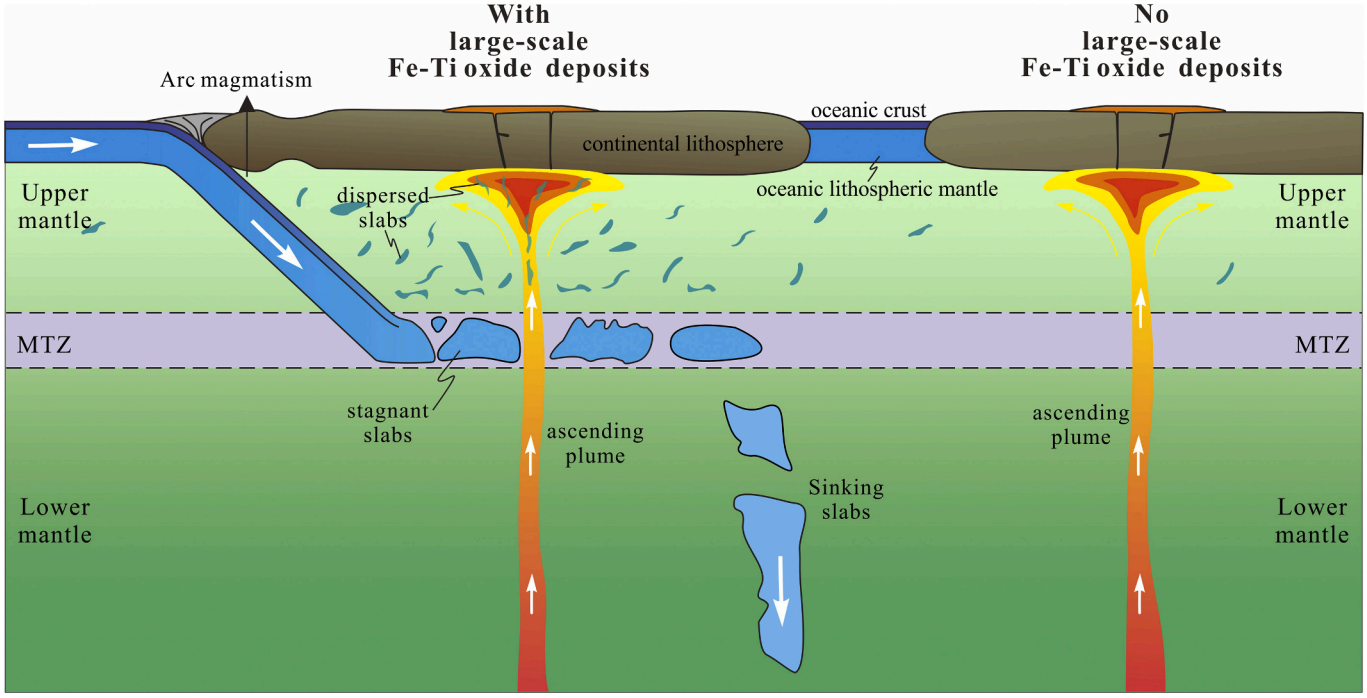

Fig. 14. A proposed genetic model for large-scale Fe–Ti-oxide deposits in LIPs with regard to long-term oceanic subduction either contemporaneous with or shortly before plume activity and adjacent to the plume region. Only very small amounts of recycled oceanic crust in the lower mantle or the core–mantle boundary can return to the base of the lithosphere owing to the buoyancy barrier, especially at the top of the mantle transition zone (Dannberg and Sobolev, 2015). Recycled oceanic crust that is dispersed in the upper mantle as a result of long-term subduction shortly before plume activity preferentially melts to produce mainly Fe-rich mafic rocks and Fe–Ti-oxide deposits in LIPs.

and consequent large-scale Fe–Ti-oxide deposits in LIPs. In general, OIBs, which are the most common mafic rocks involved in mantle plume activity, are characterized by high TiO_2 contents, and the ferropicrites that are typically found in Proterozoic–Phanerozoic LIPs also have high TiO_2 contents (1.6–3.5 wt%; Gibson, 2002 and references therein), which can be explained in terms of the presence of subducted oceanic slab materials in mantle plumes (Gibson, 2002; Prytulak and Elliott, 2007; Tuff et al., 2005). The primary magma of Wajilitag mafic rocks was enriched in FeO^T (12.1–14.5 wt%) and TiO_2 (2.02–3.91 wt%), consistent with the involvement of Si-poor pyroxenite/eclogite in the mantle source. Analogously, recycled oceanic crust in the mantle source might also account for the genesis of Fe–Ti-oxide deposits in the Panzhihua intrusions of the Emeishan LIP (Bai et al., 2014; Tang et al., 2021; Zhong et al., 2011) and the Bushveld complex (Wilson, 2012).

At mantle depths, recycled oceanic crust should be transformed into either Si-poor or Si-rich pyroxenite/eclogite (Herzberg, 2011). The solid-state interaction between MORB and peridotite would produce Si-rich pyroxenite in the upper mantle and Si-poor pyroxenite in the lower mantle, whereas cumulates of dunites, troctolites, and high-MgO gabbros in the recycled oceanic crust would produce Si-poor pyroxenite after recycling into the upper mantle (Herzberg, 2011; Lambart et al., 2013). The melts derived from Si-rich pyroxenite/eclogite are similar to peridotite melts (Lambart et al., 2013) in FeO^T but have lower FeO^T contents than those derived from Si-poor pyroxenite/eclogite. Therefore, it is probably Si-poor pyroxenite/eclogite in the mantle source that accounts for the generation of Fe–Ti-rich primary magma and consequent large-scale Fe–Ti-oxide deposits. As a fusible component (Gibson, 2002), recycled oceanic crust is preferentially melted as a result of the heat provided by a mantle plume and decompression of the upwelling asthenosphere, which can produce overall Fe-rich melts. Subducted slabs in the mantle will be folded, stretched, and thinned through convective mixing and stirring processes (Herzberg, 2011 and references therein). Thus, recycled oceanic crust can remain in the depths ranging from the upper mantle to lower mantle. Therefore, mantle sources for plume-related OIBs contain variable amounts of recycled oceanic crust (Hofmann and White, 1982), including Si-poor pyroxenite/eclogite responsible for Fe–Ti-rich primary magma and large-scale Fe–Ti-oxide deposits. However, some LIPs, such as the Siberian traps LIP (Saunders et al., 2005) and the Deccan LIP (Haase et al., 2019) show a distinct lack of large-scale Fe–Ti-oxide deposits, which would be due to the relatively low amounts of Si-poor pyroxenite/eclogite in their mantle source.

Recycled oceanic crust may be dispersed in the upper mantle (over a time scale of ~130 Myr; Richter et al., 2020) or remain within the mantle transitional zone (~20–60 Myr; Goes et al., 2017) for a long time. However, the vast majority of recycled oceanic crust will finally descend into the lower mantle and eventually reach the core–mantle boundary because it is usually denser than the surrounding mantle at shallow depths (Aoki and Takahashi, 2004). In contrast, only very small amounts of recycled oceanic crust in the lower mantle or at the core–mantle boundary can ascend to the base of the lithosphere because of the buoyancy barrier, especially at the top of the mantle transition zone (Dannberg and Sobolev, 2015). Therefore, subducted slabs dispersed in the upper mantle might provide recycled materials for basaltic rocks and Fe–Ti-oxide deposits in LIPs (Fig. 14). If so, it is reasonable to assume that the occurrence of subduction shortly prior to plume activity and near the plume region would play a crucial role in generating Fe–Ti-rich mantle sources and consequent large-scale Fe–Ti-oxide deposits (Fig. 14).

Indeed, most of the LIPs that contain large-scale Fe–Ti-oxide deposits were formed near the end of or shortly after long-term subduction in the adjacent areas (Fig. 15), as follows:

(a) Subduction processes along the Tarim Craton margin were operating at 950–215 Ma (Ge et al., 2014; Wang et al., 2020; Xiao et al., 2005; Zhong et al., 2019), which might have resulted in large amounts of recycled oceanic crust dispersed in the upper mantle throughout the duration of activity of the Tarim mantle plume at 300–270 Ma (Xu et al., 2014).

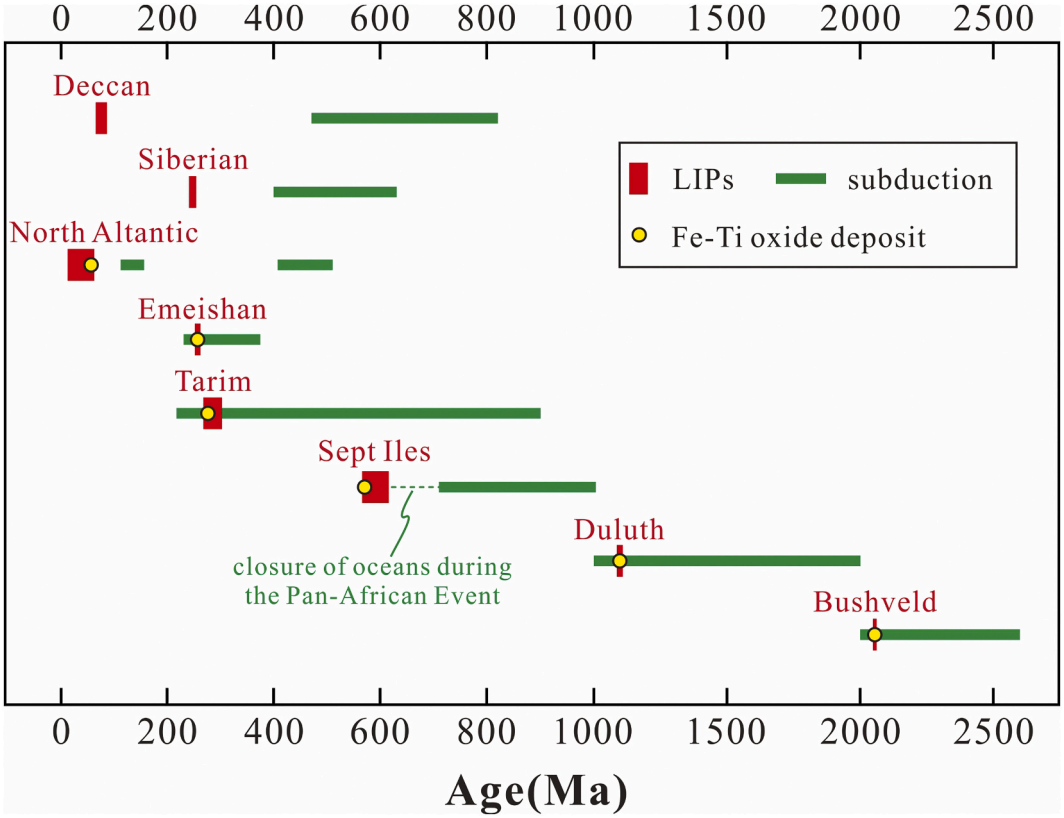

Fig. 15. Timeline of some plume-related LIPs and associated subduction events and large-scale Fe–Ti-oxide deposits. Most of the LIPs containing large-scale Fe–Ti-oxide deposits occurred at the end of or shortly after long-term subduction in adjacent areas. Literatures for the subduction timing of the LIPs are as following: Tarim (Ge et al., 2014; Wang et al., 2020; Xiao et al., 2005; Zhong et al., 2019); Emeishan (Deng et al., 2014); Bushveld (Aulbach et al., 2017; Wilson, 2012); Duluth (Karlstrom et al., 2001); Sept Iles (Cawood et al., 2010; Scotese, 2009); North Altantic (Richter et al., 2020; Shephard et al., 2016); Deccan (Yin and Harrison, 2000); Siberia (Ivanov et al., 2008; Şengör and Natal'in, 1996).

(b) The period of activity of the Emeishan plume (ca. 260 Ma) was within the duration of eastward subduction of the Tethyan oceanic plate under the Yangtze block (374–230 Ma; Deng et al., 2014). Accordingly, zircon $\delta^{18}O$ values of the Taihe Fe–Ti–V-oxide ore deposits (4.1‰–4.6‰; Tang et al., 2021) and Panzhihua clinopyroxene (3.9‰–5.4‰; Zhang et al., 2009) in the Emeishan LIP are lower than those of normal mantle-derived magmas, which indicates the involvement of newly subducted high-temperature altered oceanic crust in their source (Bai et al., 2014; Tang et al., 2021).

(c) Similarly, the mantle source for the ca. 2.06 Ga Bushveld complex, which contains giant Fe–Ti-oxide deposits, was likely affected by 2.9–2.0 Ga oceanic subduction events (Wilson, 2012), which resulted in the amalgamation of the continental nucleus (Aulbach et al., 2017).

(d) The Duluth complex in the southern margin of the Superior Craton was emplaced at ~1.1 Ga as a result of activity of the Keweenaw mantle plume (Hutchinson et al., 1990). The southeastern and southern margins of the Superior Craton (Laurentia) were the loci of prolonged subduction, accretion, and collision processes (2.0–1.0 Ga; Karlstrom et al., 2001).

(e) The ca. 565 Ma Sept Iles complex (Quebec, Canada) along the eastern margin of Laurentia was associated with the opening of the Iapetus Ocean (Cawood et al., 2010; Higgins and van Bremen, 1998; Namur et al., 2010), but the subduction–accretionary system along this margin of Laurentia was much earlier (1030–710 Ma; Cawood et al., 2010). However, during the assemblage of the Pannotia supercontinent in a Pan African event, the closure of a wide (>5500 km) ocean between South Rodinia (i.e., the Laurentia, Amazonia, Baltica, Siberia, and West Africa continents) and the Congo continent (e.g., Scotese, 2009) might have transported abundant recycled oceanic crust into the asthenosphere under eastern Laurentia.

(f) The 55 Ma Skaergaard complex (Namur et al., 2010) in the North Atlantic Igneous Province (NAIP) is located in eastern Greenland. Regional subduction events during the middle Jurassic–early Cretaceous resulted in the closure of the South Anuyi–Angayucham Ocean (Shephard et al., 2016). The proposed oceanic slabs might have been buried under present-day central Greenland at a depth of 1300–1500 km (Shephard et al., 2016) or preserved in the upper mantle beneath the Western Gakkel Ridge, Arctic Ocean (Richter et al., 2020), and could have been involved in the mantle source of the NAIP and given rise to Fe–Ti-oxide deposits in the Skaergaard complex.

In contrast, the formation of the Deccan LIP by movement of the Indian Craton over the Réunion mantle plume at 68.5–65.4 Ma (Haase et al., 2019) was much later than the subduction events recorded in the Indian Craton (Fig. 15). From the early Ordovician to Paleocene, the northern margin of the Indian Craton, as a passive continental margin, was essentially unaffected by subduction (Yin and Harrison, 2000). Thus, the presence of recycled oceanic crust in the upper mantle under the Indian lithosphere would have been negligible during the period of activity of the Deccan LIP, meaning that the mantle source would have been deficient in Fe and Ti. For the case of the Siberian Traps LIP (STLIP) at ca. 250 Ma (Saunders et al., 2005), the late Neoproterozoic to Paleozoic CAOB was located in the south of the Siberian Craton (Şengör and Natal'in, 1996). Because the CAOB was relatively far away from the Siberian Craton during the Paleozoic (Şengör and Natal'in, 1996), the subducted slabs might have stagnated in the mantle transition zone

under the thick cratonic lithosphere (Ivanov et al., 2008). The stagnating slab could have released water to create a water-saturated source for the volumetrically dominant low-Ti rocks of the STLIP (Ivanov et al., 2008), but might not have contributed additional Fe and Ti to the mantle source owing to the effect of buoyancy barrier at the top of the mantle transition zone (Dannberg and Sobolev, 2015).

6. Conclusion

Mafic–ultramafic rocks of the Wajilitag area, including clinopyroxenite, diabase, and gabbro, were formed simultaneously at ca. 280 Ma during the last magmatic episode of the Tarim Large Igneous Province and were derived from the same magmatic system.

The Wajilitag mafic–ultramafic rocks are enriched mainly in Fe and Ti and have high Fe/Mn ratioowing to the involvement of Si-poor pyroxenite in the mantle source. Long-term subduction events along the Tarim Craton margins caused large volumes of recycled oceanic crust and sediments to be transported to mantle depths to form Si-poor pyroxenite.

Subducted slabs dispersed in the upper mantle preferentially melt to produce mainly Fe-rich magma in LIPs during mantle plume activity. The occurrence of an oceanic subduction event adjacent to a mantle plume and just prior to plume activity plays a crucial role in the formation of large-scale Fe–Ti-oxide deposits in LIPs.

Supplementary data to this article can be found online at https://doi.org/10.1016/j.lithos.2021.106355.

Declaration of Competing Interest

The authors declare that they have no known competing financial interests or personal relationships that could have appeared to influence the work reported in this paper.

Acknowledgements

We thank X.R. Liang, J.L. Ma, X.P. Xia, X.L. Tu and L. Zhang for their assistance with the analyses. We are grateful to Prof. H. Zhong and an anonymous reviewer for their careful reviews and constructive comments, and thank Prof. X.H. Li for his editorial handling of this paper. This study is financially supported by the Strategic Priority Research Program (B) of the Chinese Academy of Sciences (XDB18020204), the National Natural Science Foundation of China (NSFC Projects 41625007, 41703033, 42021002), and the Key Special Project for Introduced Talents Team of Southern Marine Science and Engineering Guangdong Laboratory (Guangzhou) (GML2019ZD0202). This is contribution No. IS-3048 from GIGCAS.

References

An, M.J., Shi, Y.L., 2006. Lithospheric thickness of the Chinese continent. Phys. Earth Planet. Inter. 159, 257–266.
Aoki, I., Takahashi, E., 2004. Density of MORB eclogite in the upper mantle. Phys. Earth Planet. Inter. 143–144, 129–143.
Aulbach, S., Jacob, D.E., Cartigny, P., Stern, R.A., Simonetti, S.S., Wörner, G., Viljoen, K. S., 2017. Eclogite xenoliths from Orapa: ocean crust recycling, mantle metasomatism and carbon cycling at the western Zimbabwe craton margin. Geochim. Cosmochim. Acta 213, 574–592.
Bai, Z.J., Zhong, H., Li, C., Zhu, W.G., He, D.F., Qi, L., 2014. Contrasting parental magma compositions for the Hongge and Panzhihua magmatic Fe-Ti-V oxide deposits, Emeishan large Igneous Province, SW China. Econ. Geol. 109, 1763–1785.
Canil, D., Bellis, A.J., 2007. Ferric iron in $CaTiO_3$ perovskite as an oxygen barometer for kimberlite magmas II: applications. J. Petrol. 48, 231–252.
Cao, J., Wang, C.Y., Xing, C.M., Xu, Y.G., 2014. Origin of the early Permian Wajilitag igneous complex and associated Fe–Ti oxide mineralization in the Tarim large Igneous Province, NW China. J. Asian Earth Sci. 84, 51–68.
Cao, J., Tao, J., Wang, X., 2017. SHRIMP zircon U-Pb ages of the Wajilitag igneous complex: constraints on the origin of A-type granitoids in the Tarim large Igneous Province, NW China. Acta Geol. Sin. (English Edition) 91, 2318–2320.
Cawood, P.A., Strachan, R., Cutts, K., Kinny, P.D., Hand, M., Pisarevsky, S., 2010. Neoproterozoic orogeny along the margin of Rodinia: Valhalla orogen, North Atlantic. Geology 38, 99–102.
Chalokwu, C.I., Ariskin, A.A., Koptev-Dvornikov, E.V., 1996. Magma dynamics at the base of an evolving mafic magma chamber: incompatible element evidence from the Partridge River intrusion, Duluth complex, Minnesota, USA. Geochim. Cosmochim. Acta 60, 4997–5011.
Charlier, B., Namur, O., Toplis, M.J., Schiano, P., Cluzel, N., Higgins, M., 2011. Large-scale silicate liquid immiscibility during differentiation of tholeiitic basalt to granite and the origin of the Daly gap. Geology 39, 907–910.
Cheng, Z.G., Zhang, Z.C., Hou, T., Santosh, M., Zhang, D.Y., Ke, S., 2015. Petrogenesis of nephelinites from the Tarim Large Igneous Province, NW China: implications for mantle source characteristics and plume–lithosphere interaction. Lithos 220–223, 164–178.
Dannberg, J., Sobolev, S.V., 2015. Low-buoyancy thermochemical plumes resolve controversy of classical mantle plume concept. Nat. Commun. 6, 6960.
Dasgupta, R., Hirschmann, M.M., Smith, N.D., 2007. Partial melting experiments of peridotite + CO_2 at 3 GPa and genesis of alkalic ocean island basalts. J. Petrol. 48, 2093–2124.
Davis, F.A., Hirschmann, M.M., Humayun, M., 2011. The composition of the incipient partial melt of garnet peridotite at 3 GPa and the origin of OIB. Earth Planet. Sci. Lett. 308, 380–390.
Deng, J., Wang, Q., Li, G., Li, C., Wang, C., 2014. Tethys tectonic evolution and its bearing on the distribution of important mineral deposits in the Sanjiang region, SW China. Gondwana Res. 26, 419–437.
Foley, S.F., Prelevic, D., Rehfeldt, T., Jacob, D.E., 2013. Minor and trace elements in olivines as probes into early igneous and mantle melting processes. Earth Planet. Sci. Lett. 363, 181–191.
Ge, R.F., Zhu, W.B., Wilde, S.A., He, J.W., Cui, X., Wang, X., Zheng, B., 2014. Neoproterozoic to Paleozoic long-lived accretionary orogeny in the northern Tarim Craton. Tectonics 33, 302–329.
Gibson, S.A., 2002. Major element heterogeneity in Archean to recent mantle plume starting-heads. Earth Planet. Sci. Lett. 195, 59–74.
Gibson, S.A., Thompson, R.N., Dickin, A.P., 2000. Ferropicrites: geochemical evidence for Fe-rich streaks in upwelling mantle plumes. Earth Planet. Sci. Lett. 174, 355–374.
Goes, S., Agrusta, R., van Hunen, J., Garel, F., 2017. Subduction-transition zone interaction: a review. Geosphere 13, 644–664.
Haase, K.M., Regelous, M., Schöbel, S., Günther, T., Wall, H.D., 2019. Variation of melting processes and magma sources of the early Deccan flood basalts, Malwa Plateau, India. Earth Planet. Sci. Lett. 524, 115711.
Hanski, E.J., Smolkin, V.F., 1995. Iron- and LREE-enriched mantle source for early Proterozoic intraplate magmatism as exemplified by the Pechenga ferropicrites, Kola Peninsula, Russia. Lithos 34, 107–125.
He, P.L., Huang, X.L., Xu, Y.G., Li, H.Y., Wang, X., Li, W.X., 2016. Plume-orogenic lithosphere interaction recorded in the Haladala layered intrusion in the Southwest Tianshan Orogen, NW China. J. Geophys. Res. Solid Earth 121, 1525–1545.
Herzberg, C., 2011. Identification of source lithology in the Hawaiian and Canary Islands: implications for origins. J. Petrol. 52, 113–146.
Higgins, M.D., van Bremen, O., 1998. The age of the Sept Iles layered mafic intrusion, Canada: implications for the late Neoproterozoic/Cambrian history of southeastern Canada. J. Geol. 106, 421–432.
Hofmann, A.W., White, W.M., 1982. Mantle plumes from ancient oceanic crust. Earth Planet. Sci. Lett. 57, 421–436.
Hutchinson, D.R., White, R.S., Cannon, W.F., Schulz, K.J., 1990. Keweenaw hot spot: geophysical evidence for a 1.1 Ga mantle plume beneath the Midcontinent Rift System. J. Geophys. Res. Solid Earth Planets 95, 10869–10884.
Ivanov, A.V., Demonterova, E.I., Rasskazov, S.V., Yasnygina, T.A., 2008. Low-Ti melts from the southeastern Siberian Traps large Igneous Province: evidence for a water-rich mantle source? J. Earth Syst. Sci. 117 (1), 1–21.
Karlstrom, K.E., Ahall, K.I., Harlan, S.S., Williams, M.L., McLelland, J., Geissman, J.W., 2001. Long-lived (1.8–1.0 Ga) convergent orogen in southern Laurentia, its extensions to Australia and Baltica, and implications for refining Rodinia. Precambrian Res. 111, 5–30.
Kessel, R., Schmidt, M.W., Ulmer, P., Pettke, T., 2005. Trace element signature of subduction-zone fluids, melts and supercritical liquids at 120–180 km depth. Nature 437, 724–727.
Lambart, S., Laporte, D., Schiano, P., 2013. Markers of the pyroxenite contribution in the major-element compositions of oceanic basalts: review of the experimental constraints. Lithos 160–161, 14–36.
Le Maitre, R.W., Bateman, P., Dudek, A., Keller, J., Lameyre, M., Le Bas, M.J., Sabine, P. A., Schmid, R., Sørensen, H., Streckeisen, A., Woolley, A.R., Zanettin, B., 1989. A Classification of Igneous Rocks and a Glossary of Terms. Blackwell Scientific Publications, Oxford, 193 pp.
Li, X.H., Li, W.X., Li, Q.L., Wang, X.C., Liu, Y., Yang, Y.H., 2010. Petrogenesis and tectonic significance of the ~850 Ma Gangbian alkaline complex in South China: evidence from in situ zircon U–Pb dating, Hf–O isotopes and whole-rock geochemistry. Lithos 114, 1–15.
Li, X.H., Tang, G.Q., Gong, B., Yang, Y.H., Hou, K.J., Hu, Z.C., Li, Q.L., Liu, Y., Li, W.X., 2013. Qinghu zircon: a working reference for microbeam analysis of U–Pb age and Hf and O isotopes. Chin. Sci. Bull. 58, 4647–4654.
Li, Y.Q., Li, Z.L., Yu, X., Langmuir, C.H., Santosh, M., Yang, S.F., Chen, H.L., Tang, Z.L., Song, B., Zou, S.Y., 2014. Origin of the early Permian zircons in Keping basalts and magma evolution of the Tarim Large Igneous Province (northwestern China). Lithos 204, 47–58.
McDonough, W.F., Sun, S.S., 1995. The composition of the earth. Chem. Geol. 120, 223–253.
Middlemost, E.A.K., 1994. Naming materials in the magma igneous rock system. Earth Sci. Rev. 37, 215–224.

Namur, O., Charlier, B., Toplis, M.J., Higgins, M.D., Liegeois, J.P., Vander Auwera, J., 2010. Crystallization sequence and magma chamber processes in the ferrobasaltic Sept Iles layered intrusion, Canada. J. Petrol. 51, 1203–1236.
Philpotts, A., 1982. Compositions of immiscible liquids in volcanic rocks. Contrib. Mineral. Petrol. 80, 201–218.
Pilet, S., Baker, M.B., Stolper, E.M., 2008. Metasomatized lithosphere and the origin of alkaline Lavas. Science 320, 916–919.
Plank, T., Langmuir, C.H., 1998. The chemical composition of subducting sediment and its consequences for the crust and mantle. Chem. Geol. 145, 325–394.
Prytulak, J., Elliott, T., 2007. TiO_2 enrichment in ocean island basalts. Earth Planet. Sci. Lett. 263, 388–403.
Qin, K.Z., Su, B.X., Sakyi, P.A., Tang, D.M., Li, X.H., Sun, H., Xiao, Q.H., Liu, P.P., 2011. SIMS Zircon U–Pb geochronology and Sr–Nd isotopes of Ni–Cu bearing mafic–ultramafic intrusions in Eastern Tianshan and Beishan in correlation with flood basalts in Tarim Basin (NW China): constraints on a ca. 280 Ma mantle plume. Am. J. Sci. 311, 237–260.
Richter, M., Nebel, O., Maas, R., Mather, B., Nebel-Jacobsen, Y., Capitanio, F.A., Dick, H. J.B., Cawood, P.A., 2020. An early cretaceous subduction-modified mantle underneath the ultraslow spreading Gakkel Ridge, Arctic Ocean. Sci. Adv. 6, eabb4340.
Rudnick, R.L., Gao, S., 2003. Composition of the continental crust. Treat. Geochem. 3, 1–64.
Saunders, A.D., England, R.W., Reichow, M.K., White, R.V., 2005. A mantle plume origin for the Siberian traps: uplift and extension in the West Siberian Basin, Russia. Lithos 79, 407–424.
Scotese, C.R., 2009. Late Proterozoic plate tectonics and palaeogeography: a tale of two supercontinents, Rodinia and Pannotia. Geol. Soc. Lond., Spec. Publ. 326 (1), 67.
Şengör, A.M.C., Natal'in, B.A., 1996. Turkic-type orogeny and its role in the making of the continental crust. Annu. Rev. Earth Planet. Sci. 24, 263–337.
Shephard, G.E., Trønnes, R.G., Spakman, W., Panet, I., Gaina, C., 2016. Evidence for slab material under Greenland and links to Cretaceous High Arctic magmatism. Geophys. Res. Lett. 43, 3717–3726.
Sleep, N.H., Ebinger, C.J., Kendall, J.M., 2002. Deflection of mantle plume material by cratonic keels. Early Earth: physical, Chemical and Biological Development. Geol. Soc. Spec. Publ. 199, 135–150.
Song, X.Y., Qi, H.W., Hu, R.Z., Chen, L.M., Yu, S.Y., Zhang, J.F., 2013. Formation of thick stratiform Fe-Ti oxide layers in layered intrusion and frequent replenishment of fractionated mafic magma: evidence from the Panzhihua intrusion, SW China. Geochem. Geophys. Geosyst. 14, 712–732.
Stracke, A., Bizimis, M., Salters, V.J.M., 2003. Recycling oceanic crust: quantitative constraints. Geochem. Geophys. Geosyst. 4 https://doi.org/10.1029/2001GC000223.
Stracke, A., Hofmann, A.W., Hart, S.R., 2005. FOZO, HIMU, and the rest of the mantle zoo. Geochem. Geophys. Geosyst. 6 https://doi.org/10.1029/2004GC000824.
Sun, S.S., McDonough, W.F., 1989. Chemical and isotopic systematics of oceanic basalts: implications for mantle composition and processes. In Magmatism in the Ocean Basins (eds. A.D. Saunders and M.J. Norry). Geol. Soc. Spec. Publ. 42, 313–345.
Tang, Q.Y., Li, C., Ripley, E.M., Bao, J., Su, T.B., Xu, S.H., 2021. Sr-Nd-Hf-O isotope constraints on crustal contamination and mantle source variation of three Fe-Ti-V oxide ore deposits in the Emeishan large igneous province. Geochim. Cosmochim. Acta 292, 364–381.
Tegner, C., Lesher, C.E., Larsen, L.M., Watt, W.S., 1998. Evidence from the rare-earth-element record of mantle melting for cooling of the Tertiary Iceland plume. Nature 395, 591–594.
Toplis, M.J., Carroll, M.R., 1995. An experimental study of the influence of oxygen fugacity on Fe-Ti oxide stability, phase relations, and mineral-melt equilibria in ferro-basaltic systems. J. Petrol. 36, 1137–1170.
Tuff, J., Takahashi, E., Gibson, S.A., 2005. Experimental constraints on the role of garnet pyroxenite in the genesis of high-Fe mantle plume derived melts. J. Petrol. 46, 2023–2058.
Vervoort, J.D., Plank, T., Prytulak, J., 2011. The Hf–Nd isotopic composition of marine sediments. Geochim. Cosmochim. Acta 75, 5903–5926.
Walter, M.J., 1998. Melting of garnet peridotite and the origin of komatiite and depleted lithosphere. J. Petrol. 39, 29–60.
Wang, P., Zhao, G.C., Han, Y.G., Liu, Q., Yao, J.L., Yu, S., Li, J.H., 2020. Timing of the final closure of the Proto-Tethys Ocean: constraints from provenance of early Paleozoic sedimentary rocks in West Kunlun, NW China. Gondwana Res. 84, 151–162.
Wei, X., Xu, Y.G., Feng, Y.X., Zhao, J.X., 2014. Plume–lithosphere interaction in the generation of the Tarim large Igneous Province, NW China: geochronological and geochemical constraints. Am. J. Sci. 314, 314–356.
Weis, D., Kieffer, B., Maerschalk, C., Pretorius, W., Barling, J., 2005. High-precision Pb-Sr-Nd-Hf isotopic characterization of USGS BHVO-1 and BHVO-2 reference materials. Geochem. Geophys. Geosyst. 6 https://doi.org/10.1029/2004GC000852.
Whitaker, M.L., Nekvasil, H., Lindsley, D.H., Difrancesco, N.J., 2007. The role of pressure in producing compositional diversity in intraplate basaltic magmas. J. Petrol. 48, 365–393.
Wilson, A.H., 2012. A chill sequence to the Bushveld complex: insight into the first stage of emplacement and implications for the parental magmas. J. Petrol. 53, 1123–1168.
Xiao, L., Xu, Y.G., Mei, H.J., Zheng, Y.F., He, B., Pirajno, F., 2004. Distinct mantle sources of low-Ti and high-Ti basalts from the western Emeishan large Igneous Province, SW China: implications for plume–lithosphere interaction. Earth Planet. Sci. Lett. 228, 525–546.
Xiao, W.J., Windley, B.F., Liu, D.Y., Jian, P., Liu, C.Z., Yuan, C., Sun, M., 2005. Accretionary tectonics of the Western Kunlun Orogen, China: a Paleozoic-early Mesozoic, long-lived active continental margin with implications for the growth of Southern Eurasia. J. Geol. 113, 687–705.
Xu, Y.G., Wei, X., Luo, Z.Y., Liu, H.Q., Cao, J., 2014. The early Permian Tarim large Igneous Province: main characteristics and a plume incubation model. Lithos 204, 20–35.
Yang, Z.F., Li, J., Liang, W.F., Luo, Z.H., 2016. On the chemical markers of pyroxenite contributions in continental basalts in Eastern China: implications for source lithology and the origin of basalts. Earth Sci. Rev. 157, 18–31.
Yin, A., Harrison, T.M., 2000. Geologic evolution of the Himalayan-Tibetan orogen. Annu. Rev. Earth Planet. Sci. 28, 211–280.
Zhang, C.L., Li, X.H., Li, Z.X., Ye, H.M., Li, C.N., 2008. A Permian layered intrusive complex in the western Tarim block, northwestern China: product of a Ca. 275 Ma mantle plume? J. Geol. 116, 269–287.
Zhang, C.L., Xu, Y.G., Li, Z.X., Wang, H.Y., Ye, H.M., 2010. Diverse Permian magmatism in the Tarim Block, NW China: genetically linked to the Permian Tarim mantle plume? Lithos 119, 537–552.
Zhang, D.Y., Zhang, Z.C., Santosh, M., Cheng, Z.G., He, H., Kang, J.L., 2013. Perovskite and baddeleyite from kimberlitic intrusions in the Tarim large Igneous Province signal the onset of an end-Carboniferous mantle plume. Earth Planet. Sci. Lett. 361, 238–248.
Zhang, D.Y., Zhang, Z.C., Mao, J.W., Huang, H., Cheng, Z.G., 2016. Zircon U-Pb ages and Hf-O isotopic signatures of the Wajilitag and Puchang Fe-Ti oxide-bearing intrusive complexes: constraints on their source characteristics and temporal–spatial evolution of the Tarim large Igneous Province. Gondwana Res. 37, 71–85.
Zhang, D.Y., Zhang, Z.C., Huang, H., Cheng, Z.G., Charlier, B., 2018. Petrogenesis and metallogenesis of the Wajilitag and Puchang Fe-Ti oxide-rich intrusive complexes, northwestern Tarim large Igneous Province. Lithos 304–307, 412–435.
Zhang, Z.C., Mao, J.W., Saunders, A.D., Ai, Y., Li, Y., Zhao, L., 2009. Petrogenetic modeling of three mafc-ultramafc layered intrusions in the Emeishan large igneous province, SW China, based on isotopic and bulk chemical constraints. Lithos 113, 369–392.
Zhang, L., Ren, Z.Y., Xia, X.P., Yang, Q., Hong, L.B., Wu, D., 2019. In situ determination of trace elements in melt inclusions using laser ablation-inductively coupled plasma-sector field-mass spectrometry. Rapid Commun. Mass Spectrom. 33, 361–370.
Zhong, H., Qi, L., Hu, R.Z., Zhou, M.F., Gou, T.Z., Zhu, W.G., Liu, B.G., Chu, Z.Y., 2011. Rhenium-Osmium isotope and platinum-group elements in the Xinjie layered intrusion, SW China: implications for source mantle composition, mantle evolution, PGE fractionation and mineralization. Geochim. Cosmochim. Acta 75, 1621–1641.
Zhong, L.L., Wang, B., Jong, K.D., Zhai, Y.Z., Liu, H.S., 2019. Deformed continental arc sequences in the South Tianshan: new constraints on the early Paleozoic accretionary tectonics of the Central Asian Orogenic Belt. Tectonophysics 768, 228169.
Zou, S.Y., Li, Z.L., Song, B., Ernst, R.E., Li, Y.Q., Ren, Z.Y., Yang, S.F., Chen, H.L., Xu, Y. G., Song, X.Y., 2015. Zircon U-Pb dating, geochemistry and Sr-Nd-Pb-Hf isotopes of the Wajilitag alkali mafic dikes, and associated diorite and syenitic rocks: implications for magmatic evolution of the Tarim large Igneous Province. Lithos 212–215, 428–442.